Signal Processing Systems
Mekelweg 4,
2628 CD Delft
The Netherlands
https://sps.ewi.tudelft.nl/

M.Sc. Thesis

Estimating Transmembrane Currents and Local Activation Times from Atrial Epicardial Electrograms

Teodor Licurici

Faculty of Electrical Engineering, Mathematics and Computer Science
Delft University of Technology

Estimating Transmembrane Currents and Local Activation Times from Atrial Epicardial Electrograms

Thesis

submitted in partial fulfillment of the
requirements for the degree of

Master of Science

in

Electrical Engineering

by

Teodor Licurici
born in Bucharest, Romania

This work was performed in:

Signal Processing Systems Group
Department of Microelectronics
Faculty of Electrical Engineering, Mathematics and Computer Science
Delft University of Technology

Delft University of Technology

Delft University of Technology
Department of
Microelectronics

The undersigned hereby certify that they have read and recommend to the Faculty of Electrical Engineering, Mathematics and Computer Science for acceptance a thesis entitled **"Estimating Transmembrane Currents and Local Activation Times from Atrial Epicardial Electrograms"** by **Teodor Licurici** in partial fulfillment of the requirements for the degree of **Master of Science**.

Dated: 11.07.2023

Chairman:

Dr. R. Remis

Committee Members:

Dr. R.C. Hendriks

Dr. D. Cavallo

Abstract

Estimating the transmembrane currents travelling through the epicardium and local activation times based on atrial epicardial electrograms can greatly help in the study of cardiac arrhythmias such as atrial fibrillation. This work focuses on the accurate estimation of the aforementioned signals and features. To do this, two least squares-based regression methods were used to estimate transmembrane currents from electrograms and then find their local activation times by searching for the maximum negative slope. The first least squares optimization method consists of using standard least squares, while the second consists of regularized least squares, by combining both lasso and ridge regression, to deal with signal sparsity and multicollinearity, respectively. Furthermore, to improve estimation results, multiresolution analyses based on wavelet decompositions and principal components analysis were used to filter out parasitic components that were present in the estimated transmembrane currents by separating them from the main activation complex of the decomposed signals.

Using these algorithms on simulated data, it was shown that promising results can be achieved for both transmembrane current estimations and LAT estimations. Several wavelet support sizes were tested on the simulated data to observe performance changes. These were compared to an already existing LAT estimation algorithm. The results mainly confirm the efficiency of the proposed methods on severely diseased tissue corrupted by conduction blocks and noise.

Preface

This thesis showcases the research and work that was done toward completing my Master's graduation project and earning the Master of Science title in Electrical Engineering. The work was done within the Signals Processing Systems Group, which is part of the Faculty of Electrical Engineering, Mathematics, and Computer Science of the Delft University of Technology. It adds to the several works in this group studying the behavior of atrial epicardial electrograms.

First, I would like to extend my full gratitude towards my project supervisor, Dr. Rob Remis, who has offered me invaluable support and guidance throughout the whole process, and to Dr. Richard Hendriks, my second supervisor, who provided plenty of constructive feedback and challenging questions. I also express my appreciation to Dr. Daniele Cavallo for being part of my thesis committee.

Second, I would also like to thank the many scientists that have worked on projects related to atrial epicardial electrograms and not only that, whose insights make up the bedrock of my thesis.

Furthermore, a lot of my gratitude goes toward my family and Maria, who have always supported me in my academic pursuit and in every life event.

Finally, I want to thank all of my close friends who helped me through tough times and motivated me when I needed it the most.

Teodor Licurici
Delft, The Netherlands
11.07.2023

Contents

Nomenclature

Abreviations

AF Atrial fibrillation

AV Atrioventricular

AP Action potential

SA Sinoatrial

CV Conduction velocity

ECG/EKG Electrocardiography

SR Sinus rhythm

EGM Electrogram

LAT Local activation time

ODE Ordinary Differential Equations

OLS Ordinary Least Squares

RLS Regularized Least Squares

MRA Multiresolution Analysis

CWT Continuous Wavelet Transform

DWT Discrete Wavelet Transform

SD Steepest descent

PCA Principal Component Analysis

PCMRA Principal Component Multiresolution Analysis

SWT Stationary Wavelet Transform

DTW Dynamic Time Warping

MSE Mean-squared Error

RMSE Root-mean-square Error

NoVM Number of Vanishing Moments

List of Figures

List of Tables

1 Introduction

The heart has the important role of pumping blood throughout our bodies while providing nutrients for the different tissues of the human body and helping eliminate waste made by those same tissues. This repeating process happens as the heart takes in oxygen-deficient blood through its right side and pumps oxygenated blood coming from the lungs back into the circulatory system. In order to achieve this pumping mechanism, the cardiac muscle cells rhythmically contract the heart walls when they are activated by an action potential (AP). These APs are triggered by the sinoatrial (SA) node, the pacemaker of the heart, which sets the heart rate. In order for the heart to contract, the APs travel through the heart tissue starting from the SA node, depolarising the transmembrane potential of cardiac muscle cells and progressively activating them.

However, this process can sometimes be affected by certain complications found in tissues of the heart. The rhythmic pumping of the heart is generated by electric currents traveling through its tissue and contracting it, but these electric pathways may be disturbed by zones of reduced conductivity or no conductivity at all. This disorder causes the heart to deviate from its rhythmic pumping, thus it is called a cardiac arrhythmia.

In this project, the studied cardiac arrhythmia type affects the atrial tissues of the heart, namely atrial fibrillation (AF) [10]. This condition reduces the ability of the heart to maintain a healthy rhythm and can lead to worse complications, such as heart failure. One of the few treatment methods for atrial fibrillation is called catheter ablation. This is an invasive surgical procedure where diseased tissue is removed by introducing a catheter all the way to the heart [11].

Hence, it is important to further study the mechanisms behind AF and how this condition influences conductivity. These can be studied with the help of epicardial electrograms (EGMs), which record the electrical activity of the heart at the epicardium, the outmost layer of the heart. One of the most significant parameters that can be studied are the local activation times (LATs), which represent the times at which the cells are activated by the APs. This constructs an ill-posed inverse problem since it is nonlinear, with high dimensions, and stochastic. Estimation of LATs may also prove problematic due to EGM fractionation, caused by far-field contributions. There are several methods used to estimate LATs, a highly relevant one being deconvolution as described in [12], which is used to compare with the results obtained using the methods proposed in this paper. This method aims to find the maximum negative deflection by estimating the transmembrane current using deconvolution and ℓ_1-norm regularization using the first-order time derivative of the transmembrane currents, however, transmembrane current estimation accuracy is not an objective.

This thesis studies the accuracy of estimating transmembrane currents from EGMs using least squares optimization on a matrix EGM model. Furthermore, it computes LATs based on these estimations by finding the steepest descent (SD) of these signals. To obtain even more accurate LAT estimations, wavelet decomposition algorithms and PCA are used to filter the transmembrane current estimations before computing the SD.

The remaining part of this thesis is structured as follows. Chapter 2 delves further into the anatomy and physiology of the heart, electrocardiograms (ECGs) and EGMs, AF, and the mathematical models describing the physiology of the heart. Moreover, it also describes how the SD is defined. Chapter 3 defines the matrix version of the EGM mathematic model, the noise extension of this model, how parasitic contributions affect the EGMs, and the transmembrane current estimation algorithms. The latter item of this list includes the deconvolution method detailed in [12], and two versions of least squares optimization for the matrix version of the EGM simulation model. Chapter 4 offers an introduction to how wavelets work, describes how the filtering based on wavelet decompositions and PCA is performed, and contains examples of how these methods work on the estimated transmembrane currents. Chapter 5 details the tissue simulation setups used to test the algorithms outlined in this project and contains the final simulation results, which are then reflected upon. Finally, Chapter 6 summarizes the main findings of this thesis and proposes directions for future work.

2 Background

This chapter is meant to provide the reader with the basic concepts upon which this work is built and, moreover, to dive into low-level concepts concerning the electrical activity of the heart and the mechanisms behind atrial fibrillation (AF). Section 2.1 elaborates on the anatomy and physiology of the heart, including its electrical activity at a cellular level. Furthermore, this section explains the methods through which the electrical activity of the heart is recorded and how it can be interpreted. Following this, Section 2.2 describes the AF process and possible treatments. Finally, Section 2.3 contains the mathematical models used to simulate the electrical activity of the atria and models that can estimate this activity.

2.1 The Human Heart: Anatomy and Physiology

2.1.1 Heart Anatomy

The heart was considered to be the center of intelligence in ancient Greece. Although this was proven to be false, the heart still plays one of the most important roles in the human body. It helps to circulate the blood throughout the whole cardiovascular system, delivering nutrients and oxygen to the various tissue and cell types, while helping in disposing of their waste at the same time. The heart is located in the medial thorax cavity, the mediastinum, weighs around 250 to 350 grams, and is roughly the size of a closed human fist. The right half of the heart deals with receiving the oxygen-deficient blood coming from the body, which then carries on into the pulmonary circuit where carbon dioxide is exchanged for oxygen inside the lungs. The left half of the heart receives oxygenated blood from the pulmonary circuit, which is then pumped back to the systemic circuit made up of body tissues, in order to supply them with oxygen and nutrients. The structure of the heart can be observed in detail in Figure 2.1. The oxygen-deficient blood enters the right atrium through the two Venae Cavae, coming from the systemic circuit, and through the coronary sinus, coming from the myocardium. It is then sent to the pulmonary system from the right ventricle. Coming out of the pulmonary system, the oxygenated blood is received by the left atrium and, subsequently, pumped back into the systemic circuit by the left ventricle. As to maintain the one-way blood flow and blood pressure, the heart has four valves, which open accordingly as the blood flows in and out. Two atrioventricular (AV) valves separate the atria and the ventricles, the pulmonary valve separates the right ventricle and pulmonary trunk, and the aortic valve separates the left ventricle and the aorta. The right AV valve is called the tricuspid valve and the left one is called the mitral (bicuspid) valve. The heart wall is composed of three layers. The outer layer is the epicardium, the middle layer is the myocardium, and the inner layer is the endocardium [13].

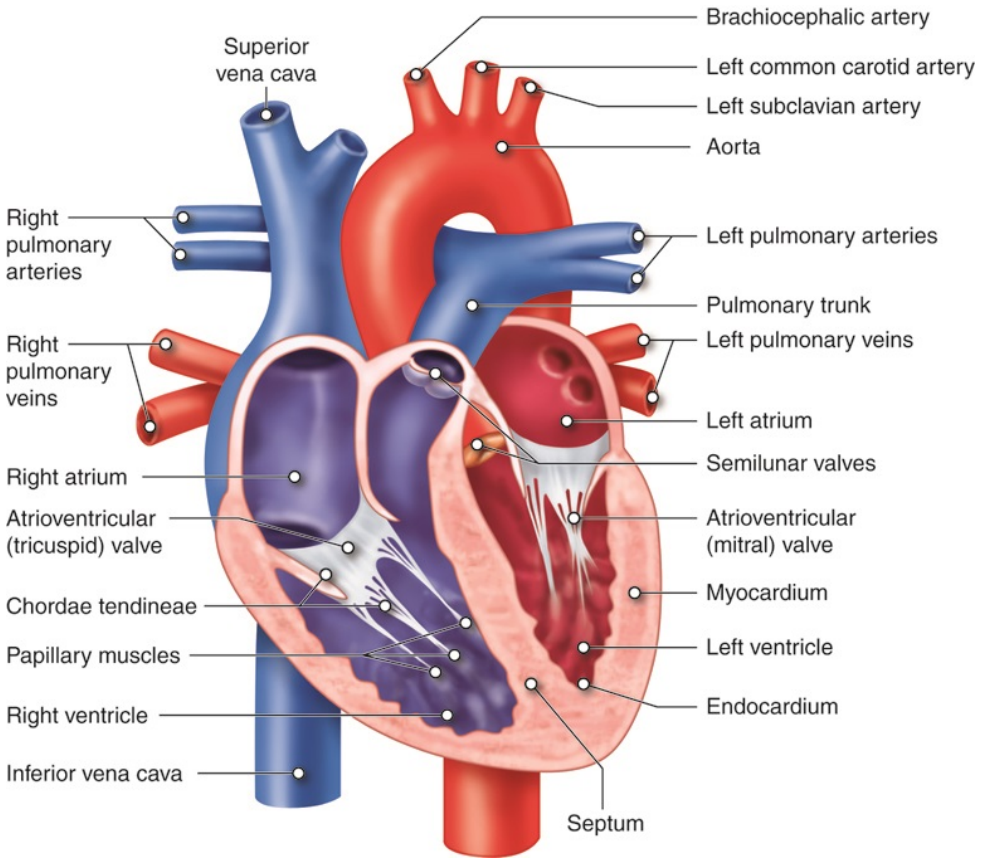

Figure 2.1: Front cross-section of the heart, depicting the main chambers and associated blood vessels. Adapted from [1].

2.1.2 Electrical Activity of the Heart

The cardiac muscle cells, also called cardiac myocytes, are short, branched, and interconnected. Most of them are contractile cells and contract during the event of depolarization triggered by an action potential (AP). The main factor that aids this process is Ca^{2+}, which is released into the cytoplasm of cardiac myocytes, triggering contractions. The heart contains two types of muscle cells, with the majority of them being contractile cardiac myocytes. However, the second type of muscle cells are the pacemaker cells, which are self-excitable and non-contractile. This means they can spontaneously depolarize, which in turn leads to the depolarization of the whole heart, thus the heart is autorhythmic. Due to the gap junctions that tie the cardiac myocytes, once one cell is excited, the rest follow, allowing the wave of depolarization to spread throughout the heart. The typical AP of a pacemaker cell can be seen in Figure 2.2, where it can be noticed that the AP generation threshold of -40mV is reached with the help of pacemaker potentials, which are the reason behind the instability of the pacemaker cells resting potential as well. Moreover, in Figure 2.3 the AP of usual contractile cardiac myocytes is depicted, where it can be seen that the depolarization causes the membrane potential to instantly go from a resting state of approximately -90mV to roughly 30mV when an AP is triggered. This peak is then continued by a plateau and finally a rapid repolarization of the membrane during the so-called absolute refractory period. The contraction period of heart myocytes matches the absolute refractory period, so the heart has enough time to relax and refill

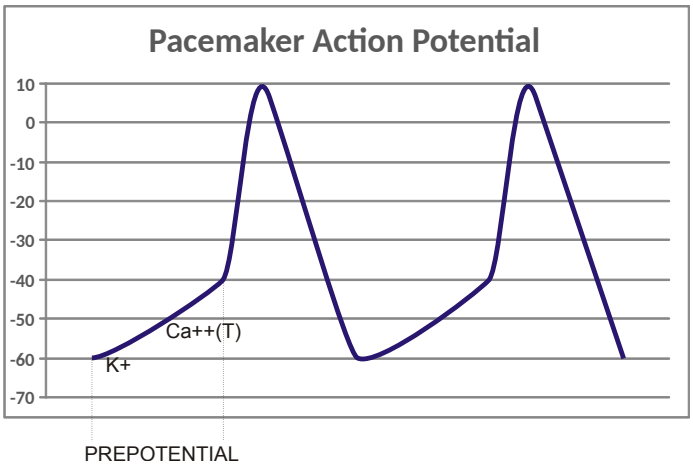

Figure 2.2: Plot depicting the AP of a pacemaker cell and the pacemaker potential. Adapted from [2].

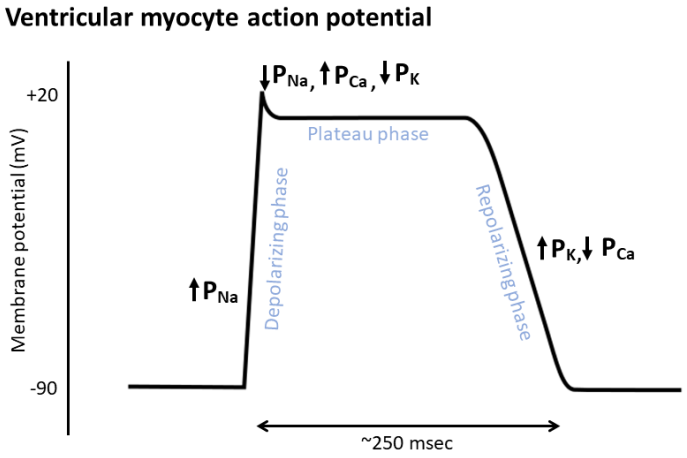

Figure 2.3: AP of a ventricular contractile cardiac muscle cell, its potential, and absolute refractory period (250ms). Adapted from [3].

[13].

The pacemaker cells are largely found in the sinoatrial (SA) and AV nodes. The excitation pathway of the heart starts at the SA node. This pathway and its steps can be fully observed in Figure 2.4. The SA node represents one of the most important regions of the heart, also named the pacemaker, having the fastest depolarization rate of the conduction system and setting the heart rate with its sinus rhythm (SR). The next element in the sequence of excitation is the AV node, where the depolarization wave is delayed by $0.1s$, permitting the atria to complete their contraction before the ventricles contract as well. The delay is caused by the smaller diameter of the muscle fibers and fewer gap junctions in this region. The depolarization wave then goes through the Common/AV bundle (or *bundle of His*), which makes up the only electrical connection between the atria

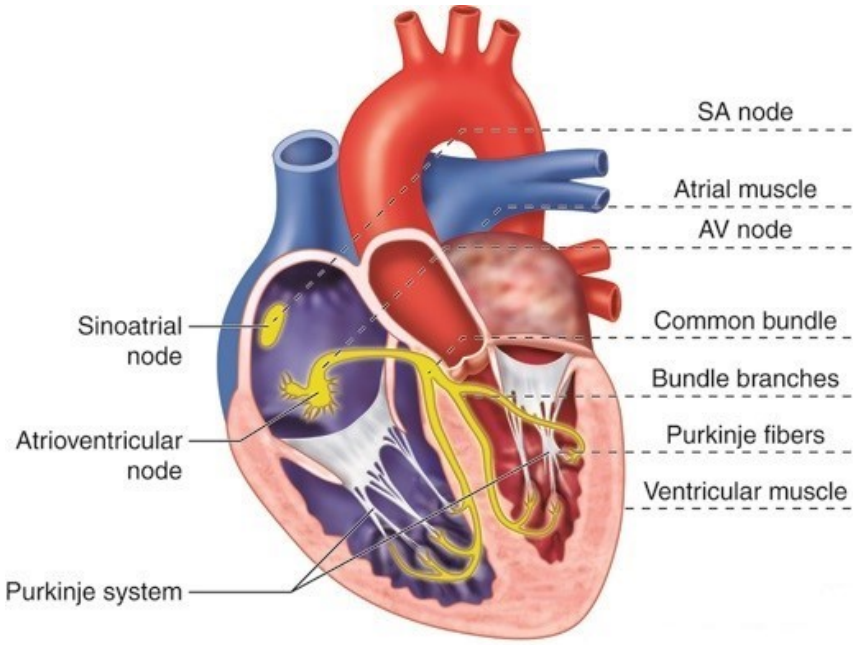

Figure 2.4: Front cross-section of the heart, describing and highlighting in yellow the sequence of excitation. Adapted from [4].

and the ventricles. Continuing the AV bundle, are the right and left bundle branches, which lead the wave towards the heart's apex. Finally, the subendocardial conducting network has the role of depolarizing the contractile cardiac myocytes of both ventricles [13].

The conduction of APs across the cardiac myocytes does not happen in an isotropic manner. It was found that signals have a higher conduction velocity (CV) longitudinally along the cardiac muscle cells. In order to quantify this phenomenon, an anisotropy ratio between the longitudinal and transversal CVs has been defined. This property is an important parameter in determining inclination towards arrhythmias [14].

2.1.3 Electrocardiograms and Electrograms

2.1.3.1 Electrocardiography

The first method for measuring the electrical activity of the heart as described earlier is electrocardiography (ECG or EKG). Through this non-invasive method, the composite of all APs fired at a certain moment in time can be measured. The machine that performs the measurements is called an electrocardiograph which records the heart's electrical activity with the help of electrodes placed on the skin of the patient. The electrodes are normally placed on the lower arms, lower legs, and across the chest wall. During a usual 12-lead ECG, three of the electrodes are used in a bipolar configuration, either between the arms or between an arm and a leg, while the other nine electrodes function in a unipolar configuration. The ECG is a useful tool and detecting acute myocardial ischemia and infarction, hypothermia, cardiac arrest, and many others [13, 15].

The typical ECG graph of the SR, along with its components, can be observed in

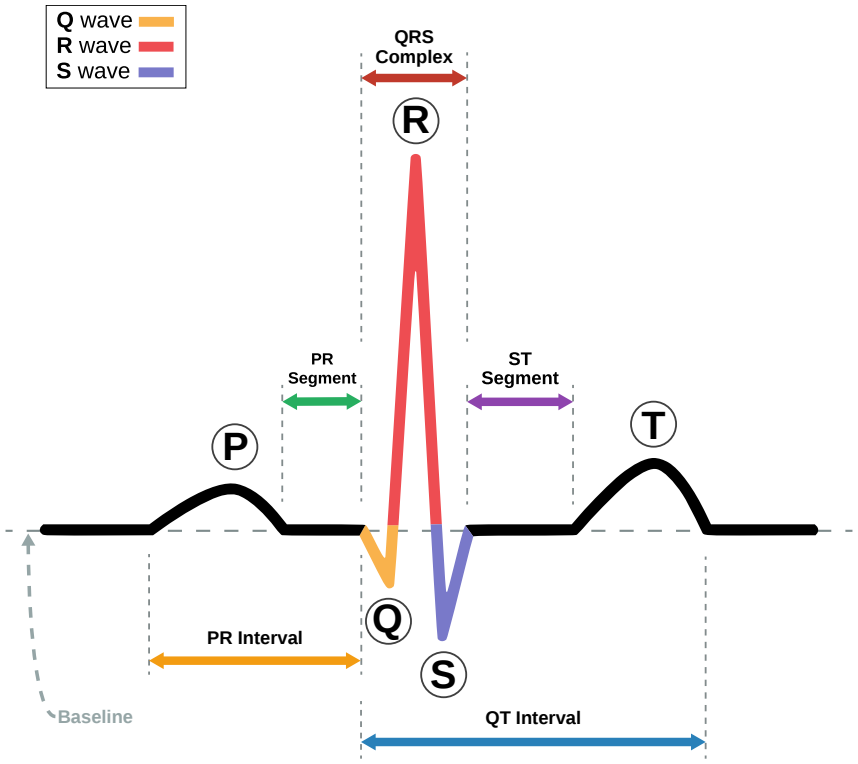

Figure 2.5: ECG graph displaying the major components of such a measurement, namely the four recognizable waveforms (P, QRS, ST, and T), the three sets of intervals (PR, QRS, and QT/QTc), and the two main segments (PR and ST). Adapted from [5].

Figure 2.5. There are five waveforms present in such a graph. The P wave marks the start of atrial depolarization, after which the aria contracts. Following this is the QRS complex corresponding to the stimulus being spread throughout the ventricles. During the ST segment, the APs reach their plateau phase, as depicted in Figure 2.3, meaning that the whole ventricular myocardium is depolarized. Immediately after, the T wave represents ventricular repolarization. Finally, atrial repolarization cannot be observed in the ECG graph since it is overshadowed by the QRS complex [13, 15].

2.1.3.2 Electrograms

Although ECGs provide a relatively easy non-invasive cardiac mapping method, the data provided by them is coarse as the heart signals have to travel through several other tissues in order to reach the body surface. Hence, a more precise method for mapping the depolarisation waves traveling through the heart comes in the form of atrial or ventricular Electrograms (EGMs). These recordings are collected by either placing a matrix of electrodes on the heart's walls during open heart surgery or by using contact catheters introduced through a large vein [16, 17]. EGMs contain local and high spatial resolution data regarding the electrical activity of the heart, as they are in direct contact with it and thus not affected by other surrounding structures. Epicardial EGMs are recorded on the outer layer of the heart wall, while endocardial EGMs are recorded on the inner layer of the heart wall.

Depending on the electrode configurations, there are mainly two types of EGMs.

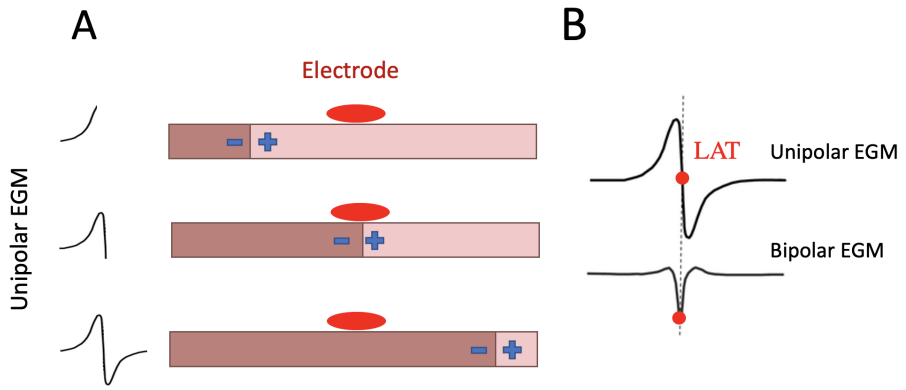

Figure 2.6: The bars in A represent a section of the myocardium as the depolarization wave passes through it and showcases how the positive wave (R-wave) and negative wave (S-wave) are recorded. A complete unipolar EGM recording can be observed in B, along a complete bipolar EGM, recorded as the difference between two closely located unipolar EGMs. Adapted from [6, p. 12].

Unipolar EGMs record the difference in electrical activity between one electrode and the reference electrode, which in most settings is connected to the Wilson Central Terminal [16]. An example of this type of recording and how it is generated can be seen in Figure 2.6, with a positive peak followed by a sudden negative deflection. As the depolarization wave nears the electrode, the positive potential is recorded, followed by a null potential as the wave is directly under the electrode, and finally the negative potential as the wave heads away from the electrode. Another type of EGM electrode configuration is bipolar recording. In order to obtain this type of EGM, two closely spaced unipolar EGMs are subtracted from each other. This process is equivalent to a high-pass spatial filter, meaning that bipolar EGMs are less susceptible to noise and far-field processes, providing a better mapping of the depolarization wave. A bipolar EGM can be observed in Figure 2.6B. Although bipolar EGMs have several advantages and are often used in clinical studies, due to their complexity they cannot be separated into their unipolar components [18]. Therefore, finding the local activation times (LATs) or interpreting spatially fractionated bipolar EGMs is a highly challenging process. Hence, when studying AF, unipolar EGMs are preferred, which are used in this thesis as well.

2.1.3.3 EGM Analysis

Several properties can be derived from an EGM in order to either characterize it, analyze wave propagation inside the tissue or any other tissue anomalies, or investigate AF. Some of the most relevant such properties are further described in this subsection.

Local activation times When the tissue is depolarized, the LAT coincides with the exact moment when the cell(s) under a specific electrode is (are) activated. This can be detected as the steepest descent in a single atrial beat EGM [19]. A more accurate derivation of the LAT can be found by looking at the steepest descent of the transmembrane current [12]. An example EGM with its LAT can be observed in Figure 2.7a.

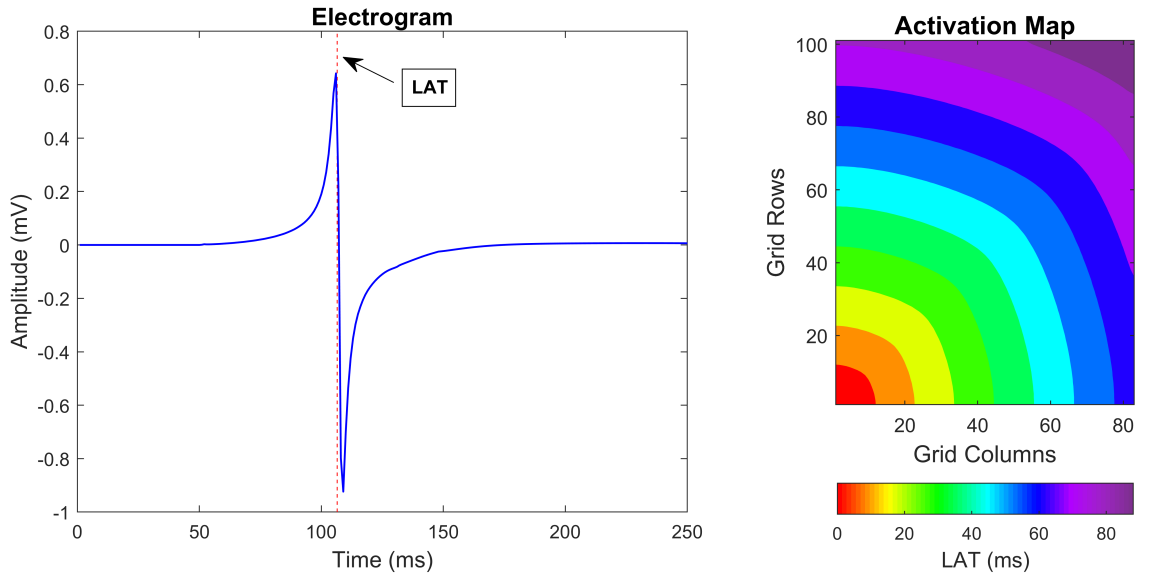

(a) (b)

Figure 2.7: Figure depicting (a) an example of a unipolar EGM with the corresponding LAT and (b) the activation map of an ideal tissue where each cell fully conducts the depolarization wave.

Activation map The activation map is a color-coded image for its corresponding matrix of electrodes, where each point represents the LAT recorded by the electrode at that location. The activation map is derived during a whole beat, where each cell goes from resting state to being activated, and then back to resting state again. An activation map example for the ideal case where each cell fully conducts the depolarizing wave can be observed in Figure 2.7b.

Slow conduction zones and conduction blocks Slow conduction zones or conduction blocks can be found in tissue areas where the absolute difference between the LATs of neighboring cells exceeds a certain threshold. Hence, the segment between them represents a problematic conduction zone.

Deflections and fractionation The deflections of an EGM represent the steep descents with an average negative slope value smaller than a certain threshold. While a normal EGM has only one deflection, a fractionated EGM can have multiple due to remote activations, inhomogeneous activations, or other artifacts [20]. Figure 2.8 displays an example of a fractionated EGM with three deflections. Such fractionated EGMs are of great importance in the study of AF occurrence and development since this EGM characteristic is one of the effects of AF.

2.2 Atrial Fibrillation

2.2.1 What is AF?

The electrical activity of the heart, as explained in the previous section, can sometimes be abnormal. Such disturbances happening during the heart's depolarization are called

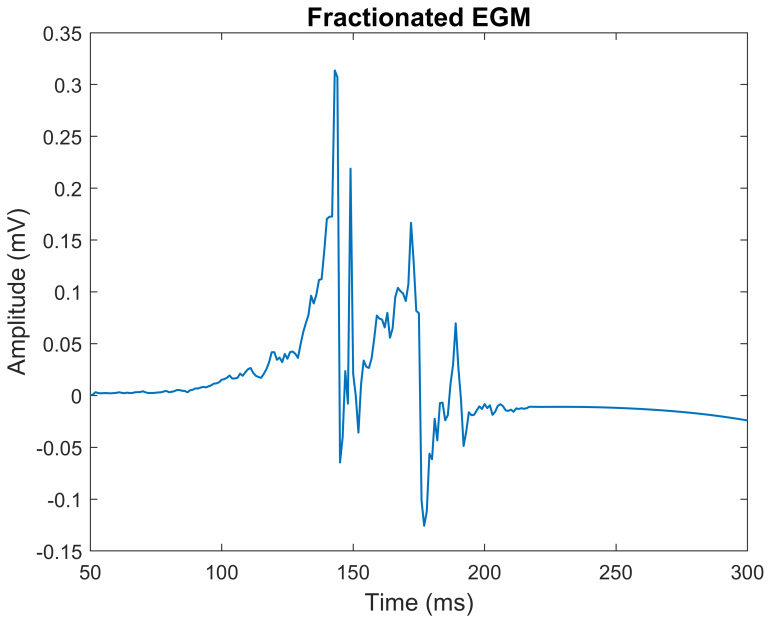

Figure 2.8: An example of a fractionated EGM with three deflections.

arrhythmia. Atrial fibrillation is a type of arrhythmia during which the atrial tissue of the heart depolarizes in a rapid and highly irregular manner. Moreover, this can lead to a similar condition in the ventricular tissue. Currently, the cause of this irregular contraction of the atria is not exactly known. It is described in [21] that roughly 1-3% of Europeans suffer from AF, mostly older people, especially with AF being an age-related condition. In its initial or short forms, AF is not necessarily dangerous and it can be asymptomatic. However, in the long run, the progression of AF can cause several complications such as blood clots, stroke, heart failure and other issues, meaning that in this case, AF has to be extensively treated [22]. Although AF is mostly found in older people or people with other heart-related comorbidities, it can also exist by itself under the name of lone AF [23].

Atrial fibrillation can be classified into three categories according to its duration and frequency of incidence. These are paroxysmal (brief and spontaneous), persistent (continuous, several tens of hours), or permanent (chronic, happening continuously, unresponsive to preventive measures) [24]. Furthermore, it was shown in [25] that paroxysmal AF can develop into longer episodes leading to an increased risk of developing other related medical conditions.

Atrial fibrillation can be diagnosed using ECGs. When AF is present, the ECG deviates from its normal parameters. Consequently, it can be observed in Figure 2.9 that during AF the intervals between the R peaks are no longer periodic, but irregular. Furthermore, P-waves are absent during AF, instead, they are replaced with low-amplitude fibrillatory waves, as the APs are misfired in the atria [26].

2.2.2 AF Mechanisms

There are many previous studies debating the mechanism behind the origin and persistence of AF, and thus many theories have been developed regarding the pathology of AF.

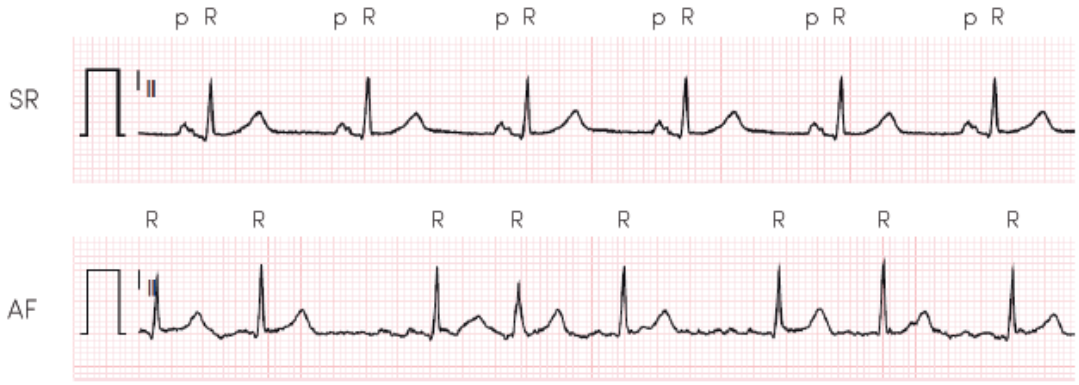

Figure 2.9: The top graph displays a regular SR, with the usual P waves and regular RR intervals. The bottom graph displays an ECG recording of AF, where the P waves are absent, the RR intervals are chaotic, and fibrillatory waves are present. Adapted from [7, p. 12].

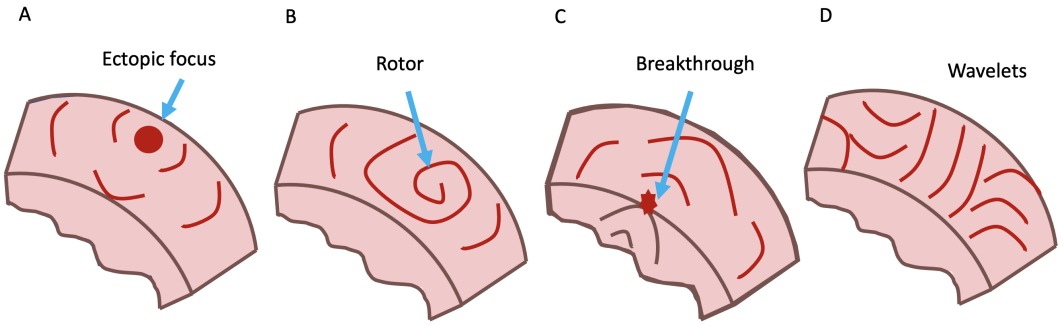

Figure 2.10: Visual representation of the four different AF mechanisms. Adapted from [6, p. 14].

The main mechanisms described in the existent literature are: ectopic foci, reentry, rotor, breakthroughs, and multiple wavelets [27].

Visual support of the aforementioned AF mechanisms can be observed in Figure 2.10. Starting with ectopic foci, this mechanism assumes that spontaneous depolarizing waves are fired from other locations than the SA and disrupt the SR (Fig. 2.10A) [27, 28]. Rotors are linked to the concept of reentry, where a wave propagates on a circular path around a conduction block, such as scar tissue, and without stopping. Rotors are however regions of functional reentry and as such they can change their position within the tissue, initiating AF (Fig. 2.10B) [28]. The endo-epicardial breakthroughs are another AF mechanism where a depolarizing wave travels unevenly through the heart muscle layers causing a spontaneous activation site in the epicardium (Fig. 2.10C) [29]. Finally, a wavelet traveling through the heart muscle could break into multiple wavelets, due to a conduction block, traveling in different directions and at contrasting velocities, corresponding to the chaotic behavior of AF (Fig. 2.10D) [30]. These interpretations regarding the mechanisms behind AF are subject to differences in recording equipment and analysis and are not necessarily contradictory between each other.

2.2.3 AF Treatment

There are mainly two ways of treating AF, early diagnosis being essential for such a condition. One way of treating AF is through medication with the other being ablation [11]. Nonetheless, ablation proved to be more efficient than drugs. Ablation therapy is a method where a catheter is introduced through blood vessels all the way to the heart. There, it is used to scar or destroy problematic areas which might be the origin of AF by either heating or cooling. There are generally four types of ablation therapy, namely pulmonary veins isolation ablation, where tissue connecting the pulmonary veins to the heart is scarred [31], atrioventricular node ablation, where chaotic atrial waves are prevented from propagating to the ventricles [32], linear atrial ablation, where long scarring lines are executed in the atria [33], and EGM guided ablation, where first problematic tissue is identified by searching for fractionated EGMs or low voltage areas, which are then ablated [34].

The lack of complete understanding towards the pathology of AF leads to restricted success rates when treating this complication. One study shows that 75% of patients were cured of AF through ablation, with the majority needing more than one surgical intervention [35]. Hence, the developemt of AF requires more research in order to develop more efficient treatment methods.

2.3 Mathematical Models

2.3.1 AP Propagation Model

In order to express the mathematical model of an EGM, first the AP mathematical model has to be explored. To do this, the cell membrane, separating the intracellular and extracellular domains, has been translated into a simplified electrical model containing a capacitor in parallel with voltage sources and resistances, corresponding to ionic channels and driving forces [36]. Hence, the capacitive current passing through a cell membrane is formulated as

$$C\frac{dV(t)}{dt} = I_{\text{st}}(t) - I_{\text{ion}}(t, V), \tag{2.1}$$

where $V(t)$ is the transmembrane potential at time instant t , $C \approx 1\mu\text{Fcm}^{-2}$ is the total membrane capacitance, I_{st} is the external stimulus current, and I_{ion} is the total ionic current, as described in the Courtemanche model [36]. A simplified circuit model of the cell membrane, as described previously, can be observed in Figure 2.11.

In order to include the flow of current and APs in the atrial tissue, the generalized cable theory or the mono-domain approach is used to further expand Eq. (2.1) [37]. In the mono-domain approach, a two- or three-dimensional grid is used to discretize the heart muscle tissue, while a reaction-diffusion equation represents the cell-to-cell depolarization wave. Furthermore, the mono-domain method assumes that both the intracellular and extracellular domains have the same anisotropy ratio. Although the mono-domain approach has certain disadvantages, such as not accounting for certain currents that can only be modeled in the bi-domain approach or not accounting for external sources (pacemaker, defibrillator), it is easier to solve and has fewer parameters. Thus, the reaction-diffusion equation for an AP propagating in 2D tissue can be modeled as

$$C\frac{dV(x_c, y_c, t_c)}{dt} = I_{\text{tm}}(x_c, y_c, t_c) + I_{\text{st}}(x_c, y_c, t_c) - I_{\text{ion}}(x_c, y_c, t_c, V), \tag{2.2}$$

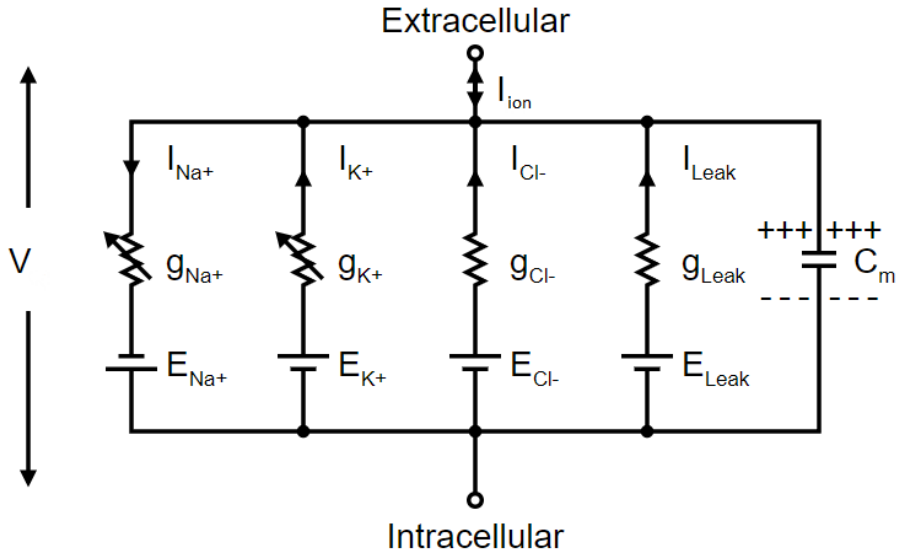

Figure 2.11: Ionic electric circuit model of the cell membrane for the AP model, where the membrane capacitance is represented by C_m, while the other four branches model the transmembrane current flow of potassium (K), sodium (Na), chloride (Cl), and other remaining ions (Leak). Adapted from [8].

where $V(x_c, y_c, t_c)$ is the per cell potential at location (x_c, y_c) and time t_c, and I_{tm} is the transmembrane current [12]. Moreover, I_{tm}, which accounts for the spatial diffusion of membrane potentials, is expressed as

$$I_{\text{tm}}(x_c, y_c, t_c) = S_{\text{v}}^{-1} \nabla \cdot \Sigma(x_c, y_c) \nabla V(x_c, y_c, t_c), \tag{2.3}$$

where $S_{\text{v}}^{-1} = 0.24 \mu\text{m}^{-1}$ is the cellular surface-to-volume ratio, $\Sigma(x_c, y_c)$ is the intracellular conductivity tensor, ∇ is the gradient operator, and $\nabla\cdot$ is the divergence operator.

2.3.2 Continuous EGM Model

The continuous EGM model can be formulated as a weighted sum of transmembrane currents, with the weights r representing the cell-to-electrode distance. Moreover, for a cell at position (x_c, y_c) and an electrode at position (x_m, y_m) at a constant height z_0 above the tissue, $r = \sqrt{(x_c - x_m)^2 + (y_c - y_m)^2 + z_0^2}$. Hence, the EGM can be formulated as

$$\Phi(x_m, y_m, t_c) = \frac{1}{4\pi\sigma_{\text{e}}} \int_{\mathcal{A}} \frac{I_{\text{tm}}(x_c, y_c, t_c)}{r} \, \mathrm{d}A(x_c, y_c) \ , \tag{2.4}$$

for $m = 1, 2, \ldots, M$ where M is the total number of electrodes, $\mathcal{A}$ is the area in which the modeled cells are located, $A(x_c, y_c)$ is the area variable, and σ_{e} the constant extra-cellular conductivity [38].

2.3.3 Discrete EGM Model

A space-discretized model is more suitable and practical in regard to the computations that are to be discussed in the following chapters of this thesis. Initially, similarly to Eq. (2.4), the model is written as

$$\Phi(\boldsymbol{y}, t) = \frac{1}{4\pi\sigma_{\mathrm{e}}} \int_{\mathcal{A}} \frac{I_{\mathrm{tm}}(\boldsymbol{x}, t)}{r} \, \mathrm{d}A(\boldsymbol{x}) \ , \tag{2.5}$$

where $\boldsymbol{y}$ and $\boldsymbol{x}$ are the location vectors of the electrodes and cells, respectively.

Subsequently, consider the array of electrodes M and $\boldsymbol{y}_m$ the location vector of electrode $m \in 1, 2, \ldots, M$, and likewise $\boldsymbol{x}_n$ for the discretized array of the N cells locations, each with an area of $a = \Delta l^2$. Furthermore, the distance $r_{m,n}$ between electrode m and cell n is formulated as

$$r_{m,n} = \sqrt{||\boldsymbol{y}_m - \boldsymbol{x}_n||^2 + \mathrm{z}_0^2}. \tag{2.6}$$

Hence, the space-discretized EGM model measured at a specific electrode m and time t is

$$\Phi(\boldsymbol{y}_m, t) = \frac{a}{4\pi\sigma_{\mathrm{e}}} \sum_{n=1}^{N} \frac{I_{\mathrm{tm}}(\boldsymbol{x}_n, t)}{r_{m,n}}. \tag{2.7}$$

2.3.4 Convolution EGM Model

In order to more easily simulate action potential propagation and EGMs, the discrete EGM model can be written as a convolution as well. The integral in Eq. (2.4) has the form of a two-dimensional spatial convolution of the transmembrane current with a distance kernel R_0 expressed as

$$R_0(x_c, y_c) = \frac{1}{\sqrt{x_c^2 + y_c^2 + \mathrm{z}_0^2}}, \tag{2.8}$$

where the electrode diameter is assumed negligible. In order to spatially sample the EGM, the sampling operator S_0 is introduced as

$$S_0(x_c, y_c) = \sum_{m=1}^{M} \delta(x_c - x_m)\delta(y_c - y_m), \tag{2.9}$$

where $\delta(x)$ is the Dirac delta impulse. Hence the continuous model in Eq.(2.4) can be written in the form of a 2D spatial convolution (operator $**$) given by [12]

$$\Phi(x_m, y_m, t_c) = \frac{1}{4\pi\sigma_{\mathrm{e}}} S_0(x_c, y_c)(R_0(x_c, y_c) ** I_{\mathrm{tm}}(x_c, y_c, t_c)). \tag{2.10}$$

Equation 2.10 can also be formulated in a matrix format. Consequently, the 3D cell grid is translated into a uniform 2D cell grid, with an inter-cell distance Δx and $N = r_{\mathrm{c}} \times c_{\mathrm{c}}$, where r_{c} and c_{c} are the number of rows and the number of columns of the grid, respectively. Moreover, Eq. (2.10) is also sampled in time with the period T_{s}, resulting in T samples. Therefore, the 2D EGM convolution model can be formulated as

$$\Phi[x, y, t] = cS_0[x, y](R_0[x, y] ** I_{\mathrm{tm}}[x, y, t]), \tag{2.11}$$

where x, y, t are the integer sampling grid indices and $c = \Delta x^2/(4\pi\sigma_{\mathrm{e}})$. Furthermore, $R_0[x, y]$ has a spatial support size of $(2\mathrm{b}+1) \times (2\mathrm{b}+1)$ and thus the 2D sampling grid has to be expanded by b samples in each direction when convoluting with the distance kernel. $S_0[x, y]$ will filter out the spatial locations where no electrodes are present by replacing them with 0 and leaving only the M locations where measurements are present.

2.3.5 Action Potential Template

It is assumed for this model that when each specific cell is activated it will generate a time-delayed version of the same stereotype AP, represented by $V_0(t)$ [6]. This results in modeling the depolarization wave as a convolution between time-delayed Dirac delta functions and $V_0(t)$. Thus, the transmembrane potential at each cell can be formulated as

$$V(x_c, y_c, t_c) = \delta(t_c - \tau_c) * V_0(t), \tag{2.12}$$

where the delay τ_c is the activation time of cell c.

2.3.6 Action Potential Propagation Model in MATLAB

The Courtemanche model is based on a set of ordinary differential equations (ODEs) that describe the dynamics of ionic currents flowing into and out of a cardiac cell, which results in the generation of an action potential. The ODEs are non-linear and require numerical integration to be solved. In the simulation, several parameters are initialized such as the capacitance of the cell, the maximal conductances of the ionic channels and the reversal potentials for each ionic current, and some initial conditions for the state variables of the model such as the membrane potential.

In the code, as described in [12], the method used to discretize the ODEs, namely the reaction-diffusion equation, is a finite difference method with no flux boundary condition. This is a numerical technique used to solve differential equations by approximating the derivatives with finite differences. The method involves dividing the domain of the problem into a grid of discrete points and approximating the derivatives at each point using the values of the function at neighboring grid points. In this case, a problem with no flux boundary condition, the boundary conditions specify that there is no flow of the solution across the boundary of the domain. This means that the solution must have a zero derivative normal to the boundary. To apply the finite difference method with no flux boundary condition, typically a central difference approximation for the derivative at the boundary points is used.

In terms of finally generating the EGM, the "point stimulation" method is used to simulate a current injection at a specific location in the cell matrix, which then calculates the voltage at other locations on the cell matrix to simulate the measurement of an extracellular potential through iteration. More specifically, first, there is the initialization of parameters for spatio-temporal sampling of the EGM: the code defines the range of rows and columns of electrodes in the recording area. A stimulating current matrix is used, where the stimulating current is present at one or more points in it, which is used to calculate the total current, including the ionic currents. The membrane potential is updated in each loop to simulate the propagation of the AP, which in turn updates the total current passing through the membrane and so on. These simulated currents are used to compute the EGMs using the discrete mathematical model described earlier. The code also calculates the ground truth LATs map, this is the time between the earliest activation of a cell (exceeding the -40mV activation threshold) and the activation of the cell that is being measured.

2.3.7 Local Activation Times Estimation

The method used to estimate LATs is the steepest descent (SD) algorithm. With SD, the LAT of a given EGM $\phi(t)$ is determined as being its global derivative minimum moment [6]. Therefore, the activation time τ of an EGM is computed using the following equation

$$\tau = \arg\min_{t} \frac{\delta\phi(t)}{\delta t}. \tag{2.13}$$

However, this method is prone to errors due to EGM fractionation. This is mainly caused by far-field influences and conduction blocks, which can lead to the SD algorithm detecting a false activation point due to the activity of other cells, other than the one(s) directly under the recording electrode, being present in the signal. This phenomenon is more thoroughly described in Section 3.1.2.

Estimating the Transmembrane Current

3

This chapter elaborates further on the discretized models that are employed to simulate EGMs. Moreover, it also describes the algorithms that are used to locally estimate the transmembrane currents from the simulated EGMs. The algorithms used for this operation are ordinary least squares (OLS) and regularized least squares (RLS). All signals are normalized before operating with them, meaning they are divided by the largest value in the data set.

3.1 Discrete EGM Matrix Model

The discretized EGM model presented in Section 2.3.3 can also be written in a matrix-vector form. Following the model described in Eq.(2.7), the inverse of the distances of all cells to electrode m can be written as $\boldsymbol{r_m} = [1/r_{m,1}, 1/r_{m,2}, \ldots, 1/r_{m,N}]$. Moreover, $c = a/(4\pi\sigma_\mathrm{e})$ which incorporates all constants is defined. Thus, the EGM model at a time instance t and electrode position m can be written as

$$\Phi(\boldsymbol{y}_m, t) = c\ \boldsymbol{r_m} \boldsymbol{i}_{tm}(t), \tag{3.1}$$

where $\boldsymbol{i}_{tm}(t) = [I_\mathrm{tm}(\boldsymbol{x}_1, t), I_\mathrm{tm}(\boldsymbol{x}_2, t), \ldots, I_\mathrm{tm}(\boldsymbol{x}_N, t)]^T$.

The next step is defining $\boldsymbol{\phi}_m = [\Phi(\boldsymbol{y}_m, 0), \Phi(\boldsymbol{y}_m, 1), \ldots, \Phi(\boldsymbol{y}_m, T-1)]$ which incorporates all T time instances in a vector for each m electrode, the $M \times N$ matrix $\boldsymbol{R} = [\boldsymbol{r_1}, \boldsymbol{r_2}, \ldots, \boldsymbol{r_M}]^T$ which stacks all of the inverse distances vectors, and the $N \times T$ matrix $\boldsymbol{I} = [\boldsymbol{i}_{tm}(0), \boldsymbol{i}_{tm}(2), \ldots, \boldsymbol{i}_{tm}(T-1)]$ with T representing the number of samples, which contains all of the transmembrane currents vectors. Hence, the matrix EGM model is formulated as

$$\boldsymbol{\Phi} = c\boldsymbol{R}\boldsymbol{I}, \tag{3.2}$$

where $\boldsymbol{\Phi} = [\boldsymbol{\phi}_1, \boldsymbol{\phi}_2, \ldots, \boldsymbol{\phi}_M]^T$ is an $M \times T$ matrix containing all M EGM measurements for each time instance.

3.1.1 Adding Noise to Recordings

The transmembrane current and implicitly, the EGM signals are simulated based on a model only accounting for the electrophysiological properties of the atrial tissues. However, when recording an EGM multiple factors can affect the signal quality such as slight equipment errors or slight tissue displacements. Hence, to have a more appropriate data set that nears real actual measurements, noise is added to the signal. The EGM model then becomes

$$\boldsymbol{\Phi}_Z = \boldsymbol{\Phi} + \boldsymbol{Z}, \tag{3.3}$$

where $\boldsymbol{Z} = [\boldsymbol{z}_1, \boldsymbol{z}_2, ..., \boldsymbol{z}_M]^T$ is a matrix containing the noise vectors in time for each electrode measurement. The noise component is modeled as additive white Gaussian

noise. Each vector component $\boldsymbol{z}_m$, where $m \in \{1, 2, \ldots, M\}$, is a time-series signal distributed as $\mathcal{N}(0, \sigma_m^2 \boldsymbol{I}_{ID})$, where $\boldsymbol{I}_{ID}$ is the identity matrix. The simulations including noise have an SNR of 10 dB. The SNR is defined as

$$SNR = \frac{||\boldsymbol{\phi}_m||_2^2}{||\boldsymbol{z}_m||_2^2}. \tag{3.4}$$

3.1.2 Parasitic Contributions and Electrogram Fractionation

In scenarios where the atrial cardiac tissue exhibits inhomogeneity or multiple excitation wavefronts propagate in the vicinity of an electrode, a phenomenon known as ectopic foci, non-local contributions from the 'distant active membrane' may be present in the EGM at a certain electrode, causing it to be significantly fractionated [39]. This happens as more distant cells can be activated at a significantly earlier time point than the ones directly under the electrode, however, the electrode can pick up contributions of the more distant cells as well. As a consequence, the LATs found through the steepest descent method, which is detailed in Section 2.3.7, may correspond to a far-field excitation rather than those of the local activity. This renders the estimation of LATs vulnerable to errors, and ultimately, this impacts the accuracy of other parameters that rely on LATs, such as conduction velocity or tissue conductivity [40]. Thus, this makes analyzing the recorded EGMs more difficult in regard to AF since the exact origin of the components is unknown [41]. However, the fractionation of an EGM can also be the cause of local inhomogeneities. The conduction blocks found in the heart's tissue are usually caused by an increased amount of collagen, which although is the structure that controls the mechanical rigidity of the heart, can separate the muscle fibers when it exceeds its healthy volume [9]. This process can be observed in Figure 3.1, where the depolarization wavefront has to follow an irregular path due to the conduction blocks caused by tissue fibrosis. A fractionated EGM example is also included in the figure which contains influences from other distant cells as well, depicting how the asynchronous activation of cardiac cells caused by diseased tissue negatively influences EGM recordings.

This being said, an important pre-processing step of EGMs before estimating the LATs directly on them is smoothing the EGM signals. This is done by sliding a moving-average filter of a certain window size across the signals.

3.2 Estimating Transmembrane Current through Deconvolution

Finding the transmembrane current I_{tm} is both a deconvolution and an interpolation problem [6]. In order to solve the deconvolution, a loss function is used, minimizing the least square error between the target value Φ and the estimated value $S_0(R_0 * * I_{\text{tm}})$. Nevertheless, this problem is ill-posed, since the number of EGMs is lower than the number of modeled cells. Hence, regularization techniques have to be used in order to make use of prior knowledge. The sharp deflection of an EGM in the context of wave propagation and AF studies can be well observed in the first-order derivative of the transmembrane current $I'_{\text{tm}}[x, y, t]$. This temporal derivative should not contain more than a few nonzero elements, represented by the fast temporal deflections. Most fractionated EGMs have a small number of deflections, thus this assumption can hold. In this case, the regularization

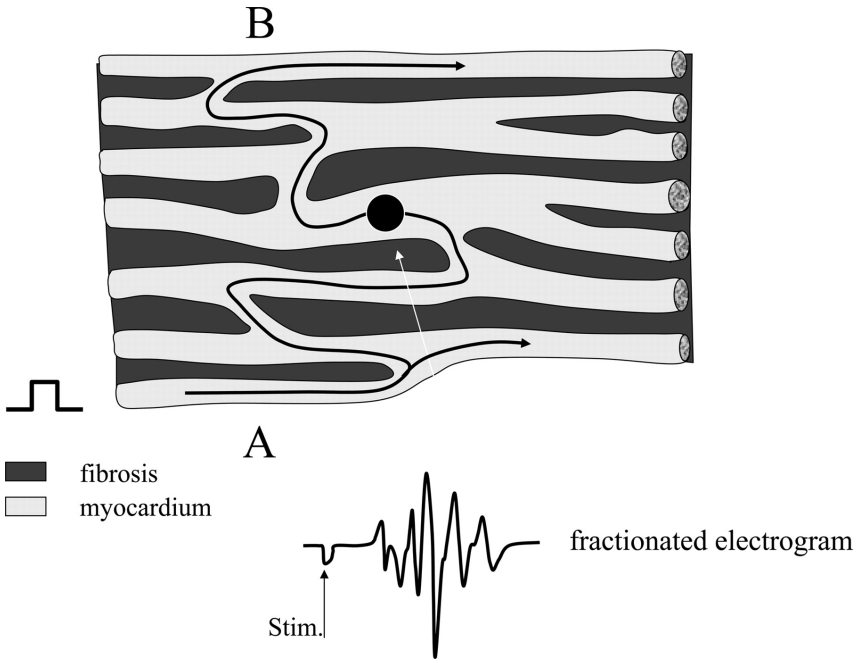

Figure 3.1: The irregular path followed by a depolarization wave through diseased tissue, where the myocardial fibers are separated by fibrosis. Due to highly erratic cell activation times caused by conduction blocks, parasitic deflections are recorded in the example EGM as well. Adapted from [9, p. 209]

function of choice is the ℓ_1-norm, since this sum of absolute values is known to induce sparsity in the solution. This will ensue in the following optimization problem as presented in [6]

$$\min_{I_{\text{tm}}} ||\Phi - S_0(R_0 * *I_{\text{tm}})||_2^2 + \lambda||I_{\text{tm}}^{'}||_1, \tag{3.5}$$

where

$$||I_{\text{tm}}||_2^2 := \sum_x \sum_y \sum_t |I_{\text{tm}}[x,y,t]|^2, \;\; ||I_{\text{tm}}^{'}||_1 := \sum_x \sum_y \sum_t |I_{\text{tm}}^{'}[x,y,t]|$$

and λ imposes the regularization weight [12]. Eq. (3.5) is a highly complex problem to solve due to the coupling between the ℓ_1-norm and ℓ_2-norm. Thus, the Split Bregman algorithm is used to split the ℓ_1-norm and ℓ_2-norm components by employing new variables [42]. The new $Z_1 = R_0 * *I_{\text{tm}}$ and $Z_2 = I_{\text{tm}}^{'}$ splitting variables are used to split the optimization problem, which then becomes

$$\begin{aligned} \min_{I_{\text{tm}},Z_1,Z_2,B_1,B_2} & ||\Phi - S_0 Z_1||_2^2 + \mu_1||Z_1 - (R_0 * *I_{\text{tm}}) - B_1||_2^2 \\ & + \lambda||Z_2||_1 + \mu_2||Z_2 - I_{\text{tm}}^{'} - B_2||_2^2, \end{aligned} \tag{3.6}$$

where B_1 and B_2 are the Bregman iterative parameters, and μ_1 and μ_2 are the penalty parameters [12].

This optimization problem can be broken into five steps, where during each step one by one the values of the unknown parameters $I_{\text{tm}}, B_1, B_2, Z_1$, and Z_2 are updated. The aim of this optimization problem is to obtain a good spatial accuracy of $I_{\text{tm}}^{'}$, hence the morphology of I_{tm} was not of importance and can drastically vary spatially.

3.3 Least Squares Optimisation to Estimate Transmembrane Current

3.3.1 Ordinary Least Squares (OLS)

A second, relatively popular algorithm used to solve an inverse problem is the OLS which involves finding the solution to a system of linear equations that minimizes the sum of the squares of the residuals, which in this case can be formulated as

$$\min_{\boldsymbol{I}} ||\boldsymbol{\Phi} - c\boldsymbol{R}\boldsymbol{I}||_2^2. \tag{3.7}$$

The solution to this optimization problem is the matrix $\boldsymbol{I}_{LS}$ that minimizes the sum of the squares of the residuals, i.e., the difference between the observed values $\boldsymbol{\Phi}$ and the predicted values $c\boldsymbol{R}\boldsymbol{I}$. Since the system described by the cell grid and electrode grid is underdetermined, as the number of cells is greater than the number of electrodes, the Singular Valued Decomposition (SVD) algorithm is used to find a solution to the OLS problem. The $\boldsymbol{R}$ matrix can be decomposed using SVD as $\boldsymbol{R} = \boldsymbol{U}\boldsymbol{\Sigma}\boldsymbol{V}^*$, where $\boldsymbol{U}$ is a size $M \times M$ unitary matrix, $\boldsymbol{\Sigma}$ is a $M \times N$ diagonal matrix with non-negative real numbers on its diagonal, $\boldsymbol{V}$ is a size $N \times N$ unitary matrix, and $\boldsymbol{V}^*$ is its Hermitian. Given this SVD, the OLS solution can be formulated as

$$\boldsymbol{I}_{LS} = c^{-1}(\boldsymbol{V}\boldsymbol{\Sigma}^{\dagger}\boldsymbol{U}^T)\boldsymbol{\Phi}, \tag{3.8}$$

where $\boldsymbol{\Sigma}^{\dagger}$ is the Moore-Penrose inverse of $\boldsymbol{\Sigma}$.

The estimated transmembrane currents using OLS can be seen in Figure 3.2c and can be compared to the initial transmembrane currents in Figure 3.2a and to the fractionated EGMs recordings in Figure 3.2b. It can be observed that the fractionated EGM contains parasitic contributions from far-field sources, which can also be found in the OLS estimation. However, the estimation is less noisy and resembles the initial transmembrane current, especially the main complex.

3.3.2 Regularized Least Squares (RLS)

Since the transmembrane current estimation system is underdetermined, a regularization parameter can be added to the OLS optimization problem to constrain the solution by penalizing the error, based on the prior knowledge that the transmembrane currents are sparse in nature and any parasitic contributions to these signals can be correlated to the main activation wave. Thus a penalty parameter is added to the linear regression problem, which embodies a combination of both ℓ_1 (lasso) and ℓ_2 (ridge regression). Hence, the OLS problem above is extended to the following equation, as presented in [43]

$$\min_{\boldsymbol{I}} \left[\frac{1}{2M} ||\boldsymbol{\Phi} - c\boldsymbol{R}\boldsymbol{I}||_2^2 + \lambda P_\alpha(\boldsymbol{I}) \right], \tag{3.9}$$

where λ is the main regularization parameter, controlling the importance of the penalty term, which is given as

$$P_\alpha(\boldsymbol{I}) = (1-\alpha)\frac{1}{2}||\boldsymbol{I}||_2^2 + \alpha||\boldsymbol{I}||_1. \tag{3.10}$$

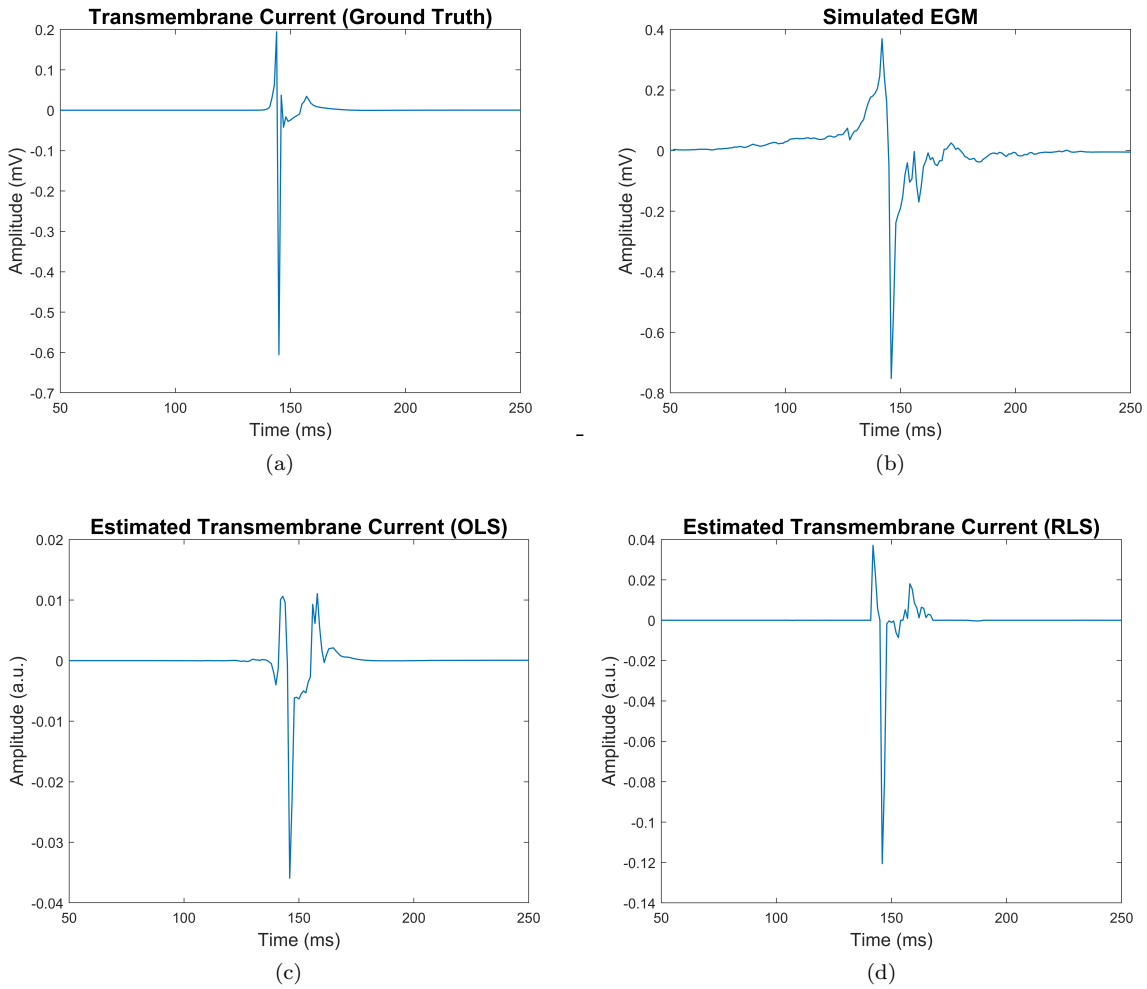

Figure 3.2: Plots of (a) the initial transmembrane current, (b) the fractionated EGM recording, (c) the estimated transmembrane current using OLS, and (d) the estimated transmembrane current using regularized least squares observed at a random position on the tissue grid.

Although the RLS optimization problem contains the EGMs and transmembrane currents in their vectorized form, the optimization is performed per each column, thus at each point in time for all electrodes and cells.

The penalty term is a combination of both lasso and ridge regression regularization. Ridge regression is ideal when all predictors are highly correlated with each other. It can help reduce the impact of multicollinearity, which can lead to unstable estimates of the regression coefficients, but also reduce the impact of outliers in the data, particularly when these influence the regression estimates. Shortly, any erratic behavior caused by high correlations in the signal is removed. Lasso instead does not take into account correlated predictors. The ℓ_1-norm promotes sparsity by assuming that most estimates are close to zero, with only a small amount being larger and non-zero.

Hence, using the elastic net described by Eq. (3.10) means that it will perform similarly to the lasso method, however, it can deal with multicollinearity as well and any erratic values caused by outliers will be removed. The α value chosen for this configuration is 0.7, meaning the lasso part of the penalty term has a greater influence, promoting

the sparse nature of the transmembrane currents, but also allowing the ridge regression part of the optimization problem to deal with multicollinearity. This suits estimating $\boldsymbol{I}$, since the signals of transmembrane currents are non-zero for only a short amount of time, corresponding to the passing of an AP, so at each point in time only a small amount of the electrodes or cells are active. Moreover, it can exclude any deflections which are considered outliers, and they can be correlated as they might originate from the same source, as in delayed contributions from other neighboring cells. The optimization problem above is then solved through coordinate descent step methods as described in detail in [43]. The main regularization parameter λ is chosen by computing a sequence of models and selecting the optimal value using 10-fold cross-validation.

The estimated transmembrane currents using regularized least squares can be observed in Figure 3.2d and can be compared to the initial transmembrane currents in Figure 3.2a and to the fractionated EGMs recordings in Figure 3.2b. While the RLS estimate does contain the extra parasitic information, which cannot be observed in the initial transmembrane current plot, the RLS estimation performs slightly better than the OLS estimation, damping the noise present in the fractionated EGM more efficiently around the main complex.

Filtering and Optimizing Transmembrane Current Estimations

4

Having obtained the transmembrane current estimations, it can be observed that these can oftentimes be heavily fractionated. Hence, a denoising method should be used to obtain better estimates, which in this case relies on wavelet transformations. This chapter describes the basic concepts behind wavelets and how they decompose a signal at several scales and resolutions. Furthermore, it explains how this decomposition can be used to perform a multiresolution analysis of a signal and why this type of analysis is beneficial for de-noising, in combination with principal component analysis (PCA). Finally, examples of filtered transmembrane current signals are illustrated to showcase the outcome of this process.

4.1 Introduction to Wavelets

The characteristics of a signal $f(t)$ can be better analyzed and processed when it is represented as a linear decomposition by

$$f(t) = \sum_{l=0}^{L} a_l \psi_l(t), \tag{4.1}$$

where l represents an integer index for the sum, a_l are the expansion coefficients, L represents the number of expansion coefficients and functions, and $\psi_l(t)$ represent a set of real-valued functions of time named the expansion set [44]. The basis, which is what this set is called if the decomposition of $f(t)$ is unique, is orthogonal when the following equation is satisfied

$$\langle \psi_k(t), \psi_l(t) \rangle = \int_0^T \psi_k(t)\psi_l(t)dt = 0 \quad k \neq l. \tag{4.2}$$

Moreover, the basis is called orthonormal if, besides being orthogonal, satisfies the following constraint as well

$$\langle \psi_k(t), \psi_l(t) \rangle = \delta(k - l), \tag{4.3}$$

meaning the basis vectors are also normalized to the unity form.

If the basis is indeed orthonormal, then the coefficients can be found using the following inner product

$$a_k = \langle f(t), \psi_k(t) \rangle = \int_0^T f(t)\psi_k(t)dt. \tag{4.4}$$

In the case of a wavelet transform, the signal expansion becomes a two-parameter system as follows

$$f(t) = \sum_{k=0}^{K} \sum_{j=0}^{J} a_{j,k} \psi_{j,k}(t), \tag{4.5}$$

where j and k are integers, and $\psi_{j,k}$ represent the wavelet transform functions, which usually construct an orthogonal basis [44]. The decomposition coefficients $a_{j,k}$ are named the discrete wavelet transform (DWT) of the signal $f(t)$ and Eq. (4.5) is the inverse DWT.

There is a significant amount of wavelet expansion sets, which can be used for certain specific signal models and share three properties [44]. First, a wavelet system is a two-dimensional decomposition set that can represent signals of different dimensionalities as shown in Eq. (4.5). Second, the wavelet transform is able to locally represent a signal in both time and frequency, unlike the Fourier transform which only localizes frequencies. This is true since the stages of the expansion go gradually from high-frequency components to lower-frequency components of the signal, while each stage is represented in the time domain. Finally, the wavelet transform is highly efficient, as most of its transforms can be computed using $O(N)$ operations, where N is the number of signal samples, which means multiplications and additions increase on a linear scale proportionally to the signal length.

The first-generation wavelet systems are derived from an initial scaling function and wavelet function by using two operations, namely scaling and translating [44]. For a wavelet function, this parameterization is obtained using a mother wavelet function $\psi(t)$ as follows

$$\psi_{j,k}(t) = 2^{j/2}\psi(2^j t - k) \quad j,k \in \mathbb{Z}, \tag{4.6}$$

where $\mathbb{Z}$ represents the set of all integers, k represents the time or space location parametrization, j represents the frequency or scale parametrization, and the factor $2^{j/2}$ helps maintaining a constant norm independent of the factor j. As k changes the location of the wavelet changes on the horizontal axis and as j changes, the shape of the wavelet changes in scale. The parameterization process is the same for the scaling function as well. In the following sections, the multiresolution principles are described, which demonstrate how a signal can be decomposed into multiple scales at different resolutions, using these parametrized versions of the scaling and wavelet functions.

A second type of wavelet decomposition is the continuous wavelet transform (CWT), used for the case where a signal is a function of a continuous variable and, thus, this transform needs to be a function of two continuous variables. Hence, the wavelet expansion then becomes

$$F(a,b) = \int_{-\infty}^{\infty} f(t) w\left(\frac{t-a}{b}\right) dt, \tag{4.7}$$

having the inverse

$$f(t) = \int_{-\infty}^{\infty}\int_{-\infty}^{\infty} F(a,b) w\left(\frac{t-a}{b}\right) dadb, \tag{4.8}$$

where $w(t)$ is the basic wavelet and $a, b \in \mathbb{R}$ represent real continuous variables.

4.1.1 Scaling Functions

The traditional notation of a scaling function is $\phi(t)$, however, since it is in conflict with the EGM notation used in this work, $\upsilon(t)$ will be used instead. A set of scaling functions can be parametrized by integer translates of the initial scaling function and is formulated as [44]

$$\upsilon_k(t) = \upsilon(t-k) \quad k \in \mathbb{Z}. \tag{4.9}$$

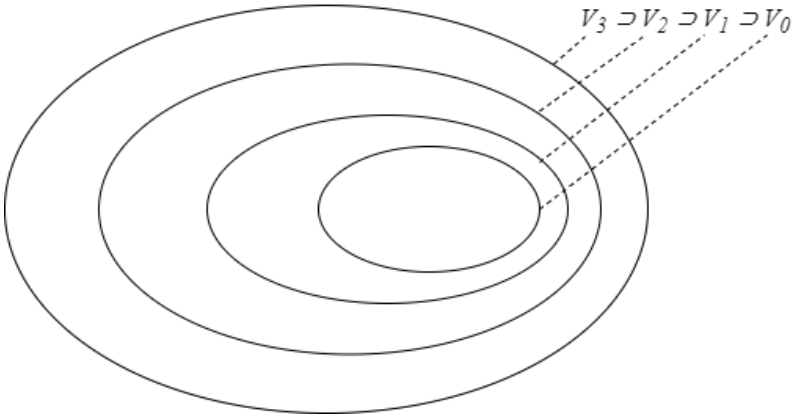

Figure 4.1: Vector spaces spanned by scaling functions, nested in order of their resolution.

Such a set of scaling functions can span a subspace V_0 described as

$$f(t) = \sum_{k=0}^{K} a_k \upsilon_k(t) \quad \forall f(t) \in V_0. \tag{4.10}$$

In order to expand a subspace generated by scaling functions, they are converted to a two-dimensional set by scaling and translation as follows

$$\upsilon_{j,k}(t) = 2^{j/2}\upsilon(2^j t - k). \tag{4.11}$$

Hence, a signal $f(t) \in V_j$ is defined as [44]

$$f(t) = \sum_{k=0}^{K} a_k \upsilon(2^j t + k). \tag{4.12}$$

4.1.2 Multiresolution Analysis

The multiresolution analysis (MRA) relies on the idea that a space containing higher-resolution signals will also include the ensuing spaces with lower-resolution signals [44]. Mathematically, this can be described by

$$V_j \subset V_{j+1} \quad \forall j \in \mathbb{Z}. \tag{4.13}$$

Following the definition of V_j, the elements of a subspace are the scaled elements of the next subspace, as in

$$f(t) \in V_j \Leftrightarrow f(2t) \in V_{j+1}. \tag{4.14}$$

This relationship is illustrated in Figure 4.1.

Due to the nesting nature of the subspaces generated by the scaling functions, it means that if $\upsilon(t) \in V_0$, it must also satisfy that $\upsilon(t) \in V_1$, the subspace spanned by $\upsilon(2t)$ [44]. Therefore, the scaling functions can be formulated as

$$\upsilon(t) = \sum_{n=0}^{N} h(n)\sqrt{2}\upsilon(2t - n), \quad n \in \mathbb{Z}, \tag{4.15}$$

where the coefficients $h(n)$ represent a sequence of numbers that make up the scaling function coefficients, with N being the total number of coefficients, while the $\sqrt{2}$ keeps the scaling function norm at two.

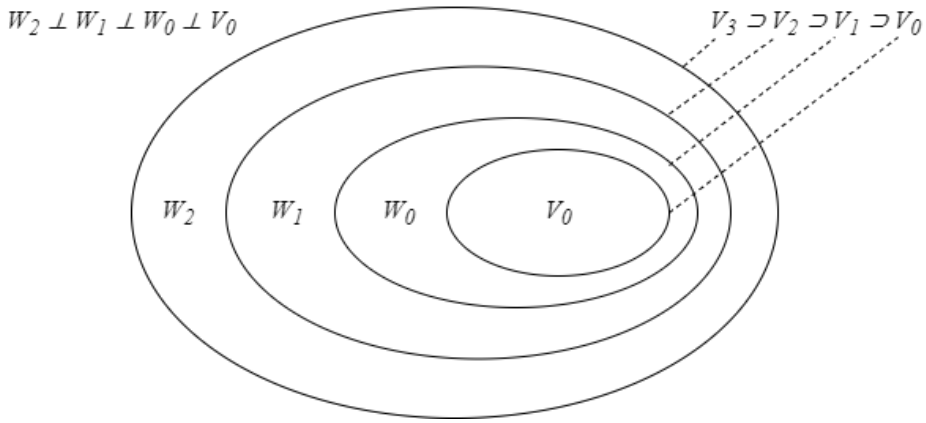

Figure 4.2: Nested scaling function and wavelet vector spaces.

4.1.3 Wavelet Functions

The relevant features of a signal are better described not by the scaling functions, but by relatively different functions $\psi_{j,k}(t)$ that contain the differences between the spaces spanned by the scaling functions [44]. These are called wavelet functions. The scaling functions and wavelets need to be orthogonal as in

$$\langle \upsilon_{j,k}(t), \psi_{j,l}(t) \rangle = \int_0^T \upsilon_{j,k}(t)\psi_{j,l}(t)dt = 0 \quad \forall j,k,l \in \mathbf{Z}. \tag{4.16}$$

This condition leads to certain advantages. A simpler calculation of the expansion coefficients is permitted by orthogonal basis functions and the signal energy is partitioned in the wavelet decomposition through Parseval's theorem [44]. A wavelet function $\psi_{j,l}(t)$ spans the subspace W_j, similarly to scaling functions.

As mentioned before, the wavelet functions span the subspaces given by the difference between the subspaces generated by the scaling functions. Thus, the coarser details described by a wavelet can be found in a space spanned by the next finer scaling function (i.e. $W_0 \subset V_1$) [44]. This property is represented in Figure 4.2.

Given the properties above, a wavelet function can be defined as a weighted sum of a finer shifted scaling function by the following equation

$$\psi(t) = \sum_{n=0}^{N} h_1(n)\sqrt{2}\upsilon(2t-n), \quad n \in \mathbb{Z}, \tag{4.17}$$

where $h_1(n)$ represents an application-specific sequence of numbers that make up the wavelet function coefficients. Furthermore, the wavelet coefficients are related to the scaling function coefficients by [44]

$$h_1(n) = (-1)^n h(1-n). \tag{4.18}$$

Finally, following the mother wavelet described in Eq. (4.17), a set of expansion functions can be formulated as observed in Eq. (4.6).

Given Eq. (4.6) and Eq. (4.11), a general expression for the expansion of a signal $g(t)$ can be formulated as [44]

$$g(t) = \sum_{k=0}^{K} c_{j0}(k)\upsilon_{j0,k}(t) + \sum_{k=0}^{K}\sum_{j=j0}^{\infty} d_j(k)\psi_{j,k}(t), \tag{4.19}$$

where the choice of j_0 represents the coarsest spanned scale, the first summation represents a coarse approximation of the signal $g(t)$ and, as j increases in the second summation, higher resolution details are added. Practically, the samples of the signals represent the finest scale. For an orthogonal wavelet system, the scaling function coefficients and wavelet coefficients can be computed as follows

$$c_j(k) = \langle g(t), \upsilon_{j,k}(t) \rangle = \int_0^T g(t)\upsilon_{j,k}(t)dt \tag{4.20}$$

and

$$d_j(k) = \langle g(t), \psi_{j,k}(t) \rangle = \int_0^T g(t)\psi_{j,k}(t)dt, \tag{4.21}$$

respectively.

4.1.4 Filter Banks

In order to observe how the wavelet coefficients decompose a signal, the relationship between the decomposition coefficients at a coarser scale can be described based on the decomposition coefficients at a finer scale [44]. Given Eq. (4.11) and Eq. (4.15), the following can be derived

$$\upsilon(2^j t - k) = \sum_{n=0}^{N} h(n)\sqrt{2}\upsilon(2^{j+1}t - 2k - n). \tag{4.22}$$

Substituting $m = 2k + n$ in the previous equation gives

$$\upsilon(2^j t - k) = \sum_{m=0}^{M} h(m - 2k)\sqrt{2}\upsilon(2^{j+1}t - m). \tag{4.23}$$

Given Eq (4.20) and Eq. (4.23), the scaling function coefficients can be written as

$$c_j(k) = \sum_{m=0}^{M} h(m - 2k) \int_0^T f(t)2^{(j+1)/2}\upsilon(2^{j+1}t - m)dt, \tag{4.24}$$

where $f(t)$ is the decomposed signal. The integral part in the previous equation represents the scaling function coefficients at scale $j + 1$ and hence

$$c_j(k) = \sum_{m=0}^{M} h(m - 2k)c_{j+1}(m). \tag{4.25}$$

Consequently, the same relationship can be derived for the wavelet coefficients as

$$d_j(k) = \sum_{m=0}^{M} h_1(m - 2k)c_{j+1}(m). \tag{4.26}$$

Equations 4.25 and 4.26 constitute digital filtering and downsampling operations [44]. In order to find the coefficients at a coarser level $j - 1$, the coefficients at scale j are convolved with the time-reversed recursion coefficients $h(-n)$ and $h_1(-n)$, followed by

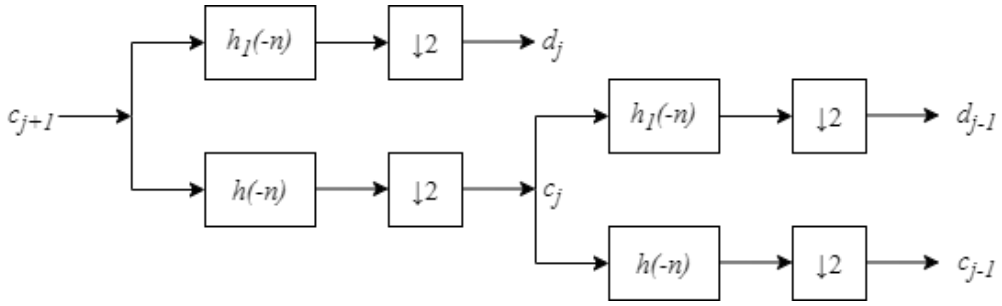

Figure 4.3: Two-scale two-band (low-pass and high-pass filtering) expansion graph.

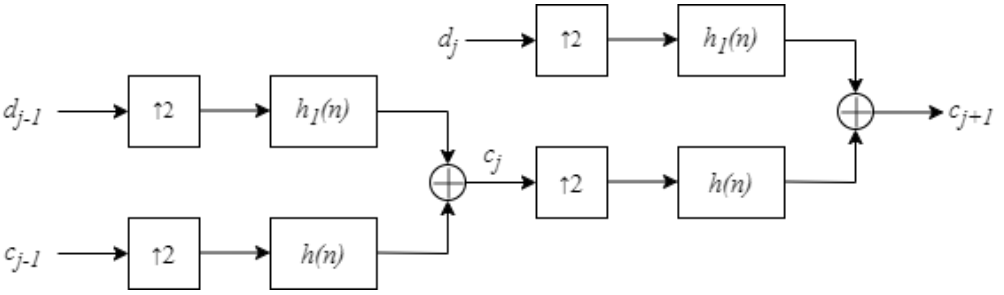

Figure 4.4: Two-scale two-band (low-pass and high-pass filtering) reconstruction graph.

downsampling them. The filter represented by $h(-n)$ is a low-pass filter, while the filter represented by $h_1(-n)$ is a high-pass filter. Each corresponds to its level of detail computation, namely the low-pass filter transitions the signal to a coarser level and the high-pass filter deals with the signal details at its corresponding scale. For ease of notation, both $h(n)$ and $h_0(n)$ will be used from now on for the scaling function coefficients. A graphical representation of the filtering and downsampling by equations 4.25 and 4.26 can be seen in Figure 4.3. There, two coarser scales are derived by iterating the two aforementioned equations. To reconstruct the initial signal from its decomposition, the opposite operations are performed. Thus, starting from the coarsest scale, the scaling function coefficients and wavelet coefficients are upsampled and then each convolved with $h_0(n)$ and $h_1(n)$, respectively. This is done repeatedly until the initial signal is finally reconstructed. This process can be observed in Figure 4.4, for a two-scale expansion.

4.2 Electrogram Multiresolution Analysis

To illustrate the wavelet decomposition process described up till now, a five-scale decomposition is performed on an estimated EGM signal using the LSQ methods described in Chapter 3, simulated on diseased tissue. A five-scale expansion was chosen, as based on multiple experiments this value yielded the optimal amount of decomposition details to observe the EGM signals for relevant parameters and filtering, and computing even coarser scales would not offer any new signal characteristics. The signal expansions performed in this work are computed using the "symlet" ("sym") wavelets family, which is a generally efficient choice for signal denoising. As an example, the initial scaling function and mother wavelet of the sym4 wavelet set can be observed in Figures 4.5a and 4.5b, respectively. The number four in the wavelet name, sym4, stands for the number of its vanishing moments. The vanishing moments of a wavelet function refer to the number

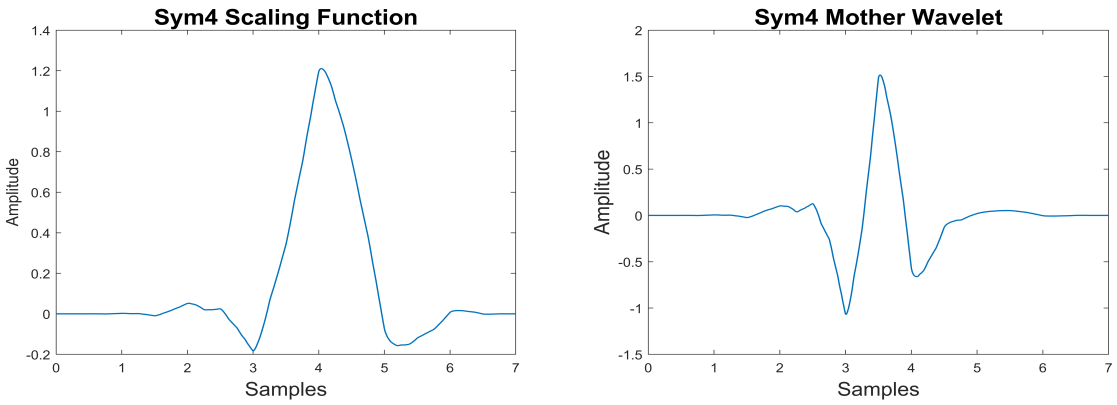

(a) (b)

Figure 4.5: Graphs depicting (a) the initial scaling function and (b) the mother wavelet of the sym4 wavelet set.

of moments of the function that are equal to zero (derivatives of the function) or its capability to represent the smoothness of a function [44]. Therefore, for closely-spaced distinct features in a signal, a wavelet with fewer vanishing moments (smaller support) is required to accurately identify them in the decomposition, given they are prominent enough, whereas, for a signal with sparsely-spaced features, wavelets with more vanishing moments can be used to distinguish the desired features of the signal. By applying the decomposition process described in the previous section, using the wavelet family displayed in Figure 4.5, a five-scale decomposition of an EGM is computed. It can be observed in Figure 4.6. The first row shows the initial signal, the following five rows represent the wavelet coefficients from fine to coarse for each of the five scales, and the last row displays the scaling function coefficients at the coarsest scale. It can be seen in Figure 4.6 that the noisy and parasitic components of the signal can be mainly found in the first two finest scales, as that is where most high-frequency information can be found. Hence, by omitting them when reconstructing the signal, a denoised version of the initial signal may be computed. However, this will be elaborated in the following sections.

4.2.1 Principal Component Multiresolution Analysis

PCA (Principal Component Analysis) is a mathematical technique used in data analysis to transform a set of correlated variables into a new set of uncorrelated variables, called principal components. The principal components are ordered in terms of the amount of variance they explain in the original data, with the first principal component explaining the largest amount of variance and each subsequent component explaining a smaller amount. PCA finds a linear combination of the original variables that best captures the variation in the data. This linear combination is called the first principal component. Subsequent principal components are found by finding linear combinations of the remaining variables that are uncorrelated with the first principal component and explaining the remaining variation in the data.

The first step in PCA is to standardize the data by subtracting the mean and dividing by the standard deviation. This is followed by computing the covariance matrix of the standardized data. The eigenvectors and eigenvalues of the covariance matrix are then

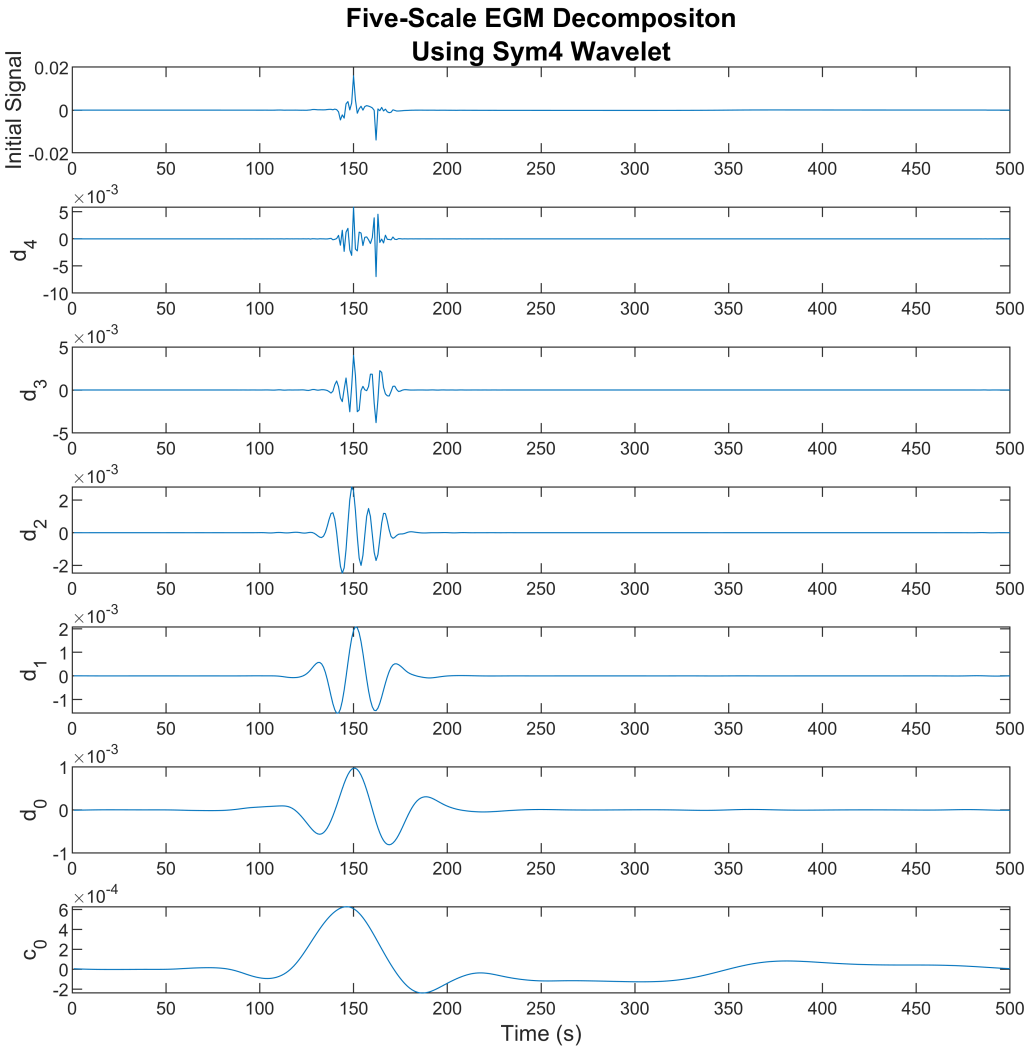

Figure 4.6: Five-scale decomposition of EGM signal simulated on diseased tissue. Starting from the top plot, the initial signal, followed by wavelet coefficients at each scale, and finally, the scaling function coefficients at the coarsest level are displayed.

derived. The eigenvectors represent the principal components of the data, while the eigenvalues represent the amount of variance explained by each principal component. By removing the appropriate amount of irrelevant principal components, signal errors can be eliminated. However, problems may occur in PCA if certain events are localized at different positions in time and frequency, or in the case of stochastic processes, with their energy changing in time and/or frequency [45].

Principal Component Multiresolution Analysis (PCMRA) is a process where the denoising procedure of a signal is improved by using PCA at each scale of the MRA of a signal and then again on the reconstructed signal, thus eliminating the influence of problems such as those described in the previous paragraph [45]. After deriving the principal components of the wavelet coefficients at each scale and on the scaling function coefficients

at the coarsest scale, only a significant set of them is kept at each scale, based on a certain thresholding method. After performing the scale-based PCA, the signal is reconstructed and PCA is again performed on it. A graphical representation of this whole process can be seen in Figure 4.7.

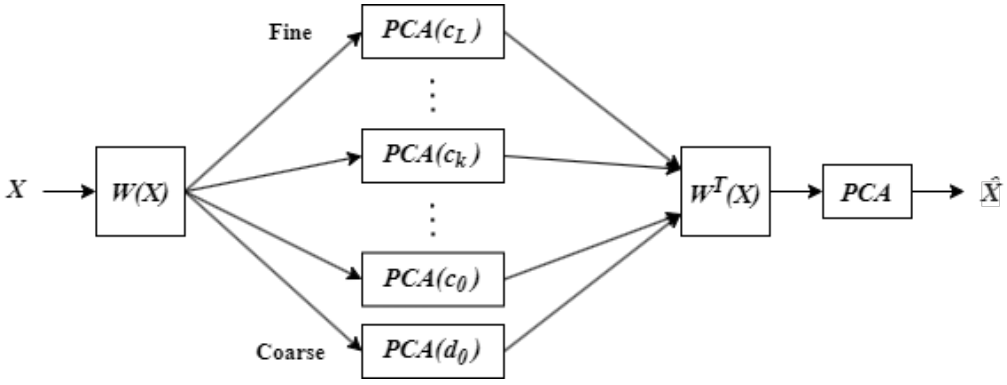

Figure 4.7: Pipeline of the PCMRA methodology, where $\boldsymbol{W}$ represents the wavelet decomposition process.

For the experiments performed in this thesis, the "symlet" wavelet family was used, testing for multiple values of vanishing moments, as it will be shown later. The contributions of the first one or two finest scales wavelet coefficients, according to noise levels, are entirely ignored, as they mostly contain noise details, while the thresholding method used for the PCA at the other scales is the Kaiser method. This means that only the components associated with eigenvalues exceeding the mean of all eigenvalues are used.

Before moving to estimate the LATs on the filtered, improved signals, they are again decomposed using the Stationary Wavelet Transform (SWT) and reconstructed after, omitting again the first one or two decomposition levels, as explained earlier. Compared to the DWT, the SWT has the property of translation-invariance, which means it better deals with artifacts that would usually appear when using the DWT around discontinuities of the decomposed signal [46]. Hence, by using the SWT, several artifacts that might appear from the PCMRA algorithm or are still present in the signals after filtering are removed. In SWT, instead of downsampling and upsampling the signal itself, the filters themselves (h and h_1) are upsampled by a factor of 2^{j-1} at each level j of the decomposition, which gives the SWT translation invariance [47]. Since the filters are of dyadic lengths (power of 2), the currents are symmetrically extended to deal with this and any border effects that might ensue. After filtering with SWT, the signals are resized to their initial length.

The filtered results can be observed in Figure 4.8. In Figure 4.8a the initial simulated transmembrane current can be observed, followed by its corresponding EGM with added white Gaussian noise in Figure 4.8b, the estimated transmembrane current in Figure 4.8c, the estimated transmembrane current after being filtered using PCMRA in Figure 4.8d, and finally the estimated transmembrane current after being filtered SWT as well in Figure 4.8e. It can be seen that going from the initial transmembrane current estimation to its final filtered form, the clarity of the signal increases with more parasitic components being removed and the signal is smoother, with a lot of noisy high-frequency components having been filtered.

Finally, the steepest descent as described earlier is used on the PCMRA and SWT filtered signal to estimate the LATs. However, this will prove to be prone to errors in certain cases, as it will be shown in the following chapter.

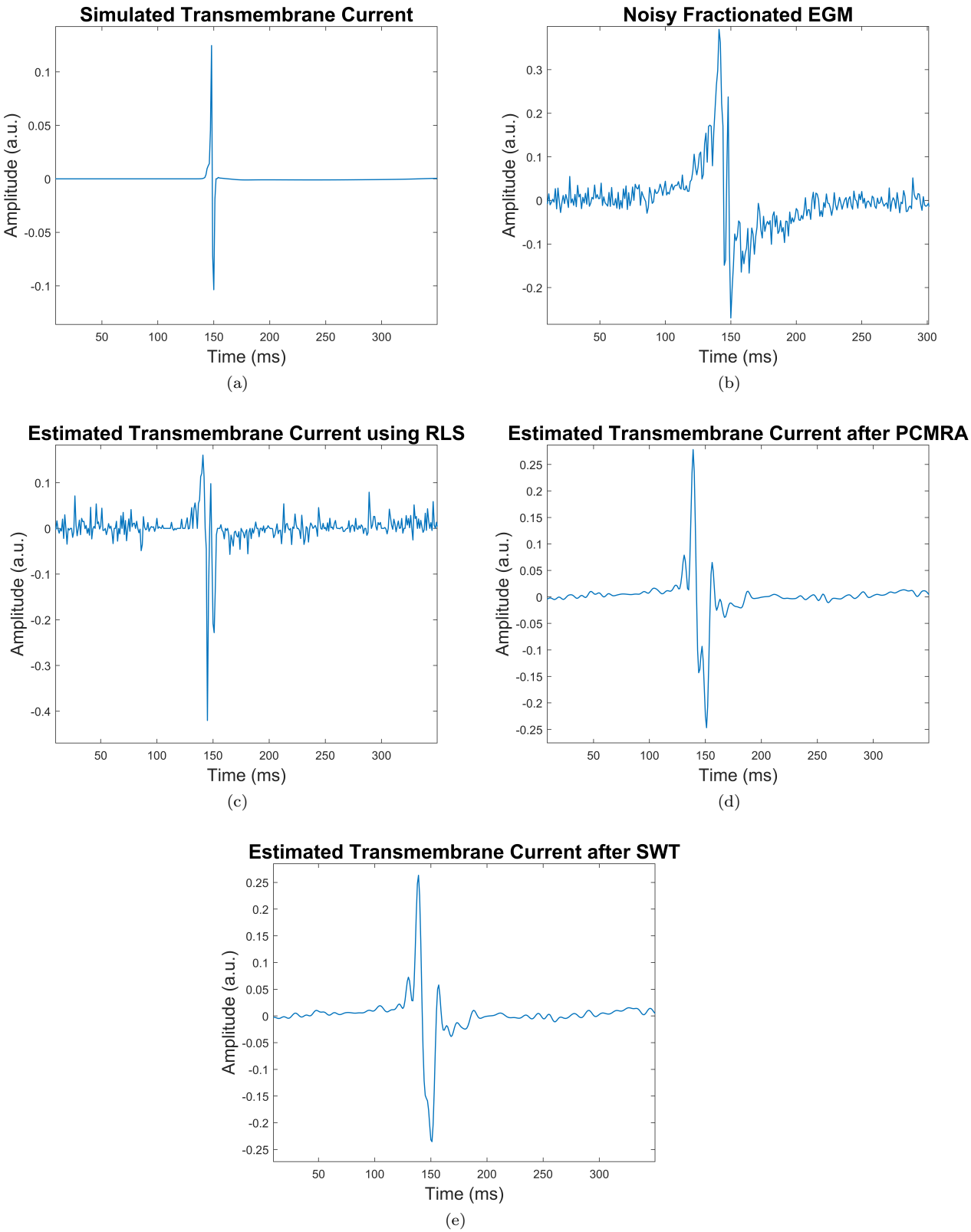

Figure 4.8: Plots depicting the (a) transmembrane current tissue level (ground truth) at a random electrode position on the grid, (b) its corresponding noisy fractionated EGM (c) the transmembrane current RLS estimation based on the EGM, (d) the transmembrane current estimation current after the first filtering stage using PCMRA, and (e) the transmembrane current estimation after the second filtering stage using SWT.

Atrial Electrical Signals Simulation Setup and Results

5

This chapter elaborates upon the types of tissues and stimulation points along the tissues that were used in order to simulate EGMs. Furthermore, it shows and discusses the estimated transmembrane currents and LATs, that were computed using the methods described in the previous chapters.

5.1 Simulation Setup for Fractionated Electrograms Generation

In order to assess the methods proposed in this thesis, two different patterns of tissue heterogeneity are used to simulate tissue conductivity maps. This is done to generate fractionated EGMs that are similar to real clinical data. The size of the tissue cell matrix is 101×83, with an inter-cellular distance of $\Delta x = 0.7$ mm.

The first type of simulated conduction pattern T1 consists of healthy, homogeneous tissue, which fully conducts the depolarization wave across it, having no zones of impaired conduction. The second heterogeneity pattern T2 consists of zones of no conduction, in the form of randomly placed lines of conduction blocks, and percolation, with randomly placed dots of conduction blocks, both of which prevent cells from coupling on the grid [48, 49]. Finally, in order to test how the algorithms perform in different scenarios, three random variations have been generated for tissue type T2(a/b/c). The first testing set-up has only one stimulation point, at the bottom left of the whole 101×83 grid, while the second set-up has three stimulation points spread across the tissue grid. The stimulation points in the latter set-up case are called ectopic foci. The conduction map of tissue type T1 can be observed in Figure 5.1, while the conduction maps of the tissue type T2 variations can be observed in Figure 5.2. The dark-blue areas are zones of no conduction. Moreover, the purple hexagram corresponds to the single stimulation point set-up, while the orange hexagrams are the stimulation points corresponding to the ectopic foci set-up.

The activation maps display the actual activation time of each cell in the 101×83 matrix, represented by the moment where the potential of the cell reaches the -40 mV during its depolarization phase. The white dots in the activation maps depict cells that were not activated due to conduction blocks. The simulated activation maps for tissue type T1 for both the single stimulation point and the ectopic foci set-ups can be seen in Figure 5.3, the simulated activation maps for the three variations of tissue type T2 for the single stimulation point set-up can be seen in Figure 5.4, and the simulated activation maps for the three variations of tissue type T2 for ectopic foci set-up can be seen in Figure 5.5. As can be seen for the single-point stimulation set-ups, the LATs are the lowest in the bottom left corner, corresponding to the red-colored area, while for the ectopic foci set-ups, the red-colored areas in the activation maps correspond to the three stimulation points for the ectopic foci setting. However, for tissue type T2c in Figure 5.5c, the bottom left stimulation point is inactive as it is located directly inside a conduction block zone.

The EGMs are generated using Eq. (2.4), in the form of Eq. (3.2), and recorded for a

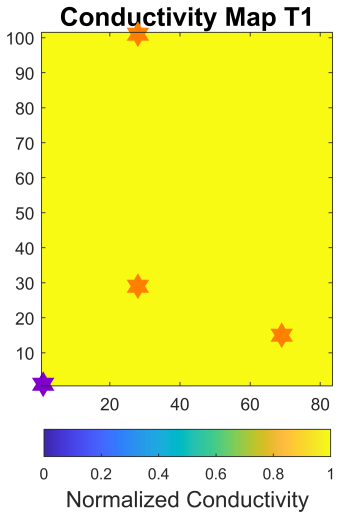

Figure 5.1: Simulated conductivity maps of the first tissue type T1. The purple hexagram represents the stimulation point in the case of a single stimulation current being applied to the tissue, while the orange hexagrams correspond to the three stimulation points in the case where multiple stimulation currents are applied to the tissue.

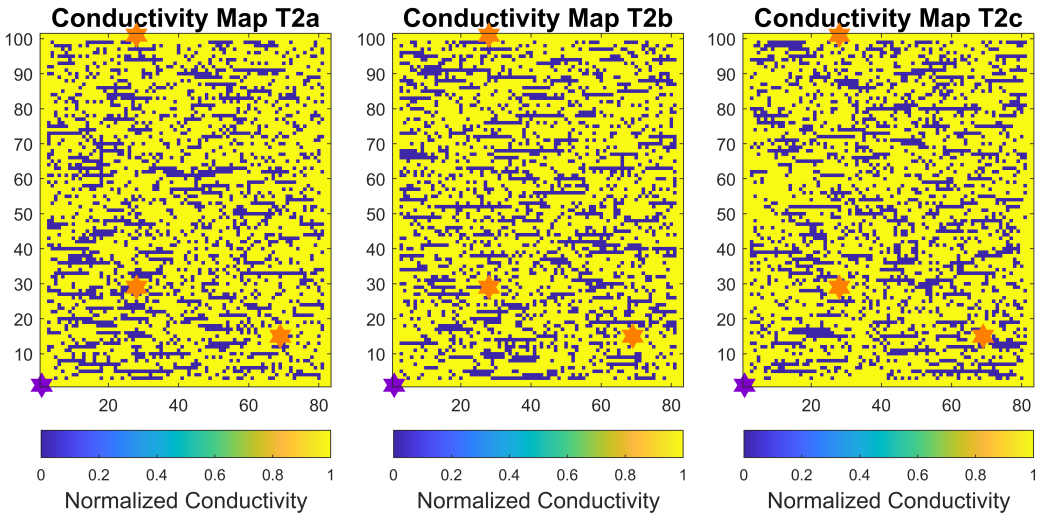

(a) (b) (c)

Figure 5.2: Simulated conductivity maps of (a) the first variation of tissue type T2, (b) the second variation of tissue type T2, and (c) the third variation of tissue type T2. The purple hexagram represents the stimulation point in the case of a single stimulation current being applied to the tissue, while the orange hexagrams correspond to the three stimulation points in the case where multiple stimulation currents are applied to the tissue.

15×9 electrode matrix, which covers an area of 43×25 central cells. This results in a total of 135 simulated EGMs. The inter-electrode distance is $\Delta y = 3\Delta x$ and the electrode matrix is assumed to be at a constant height of $z_0 = 1$ mm. The total simulation time is 500 ms and the transmembrane currents are simulated at a frequency of 20 kHz, however, the EGMs were downsampled to match a frequency of 1 kHz, which corresponds to actual

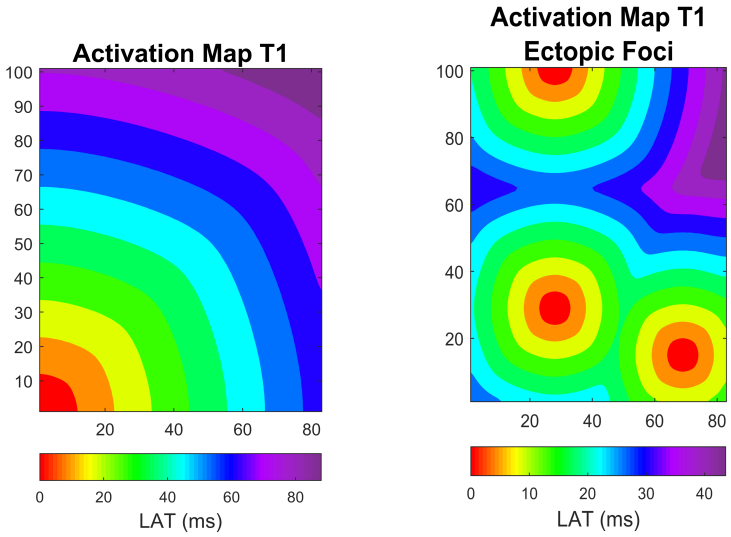

(a) (b)

Figure 5.3: Simulated activation maps of (a) tissue type T1 with one stimulation point and (b) tissue type T1 with ectopic foci. The white spots represent cells that did not activate.

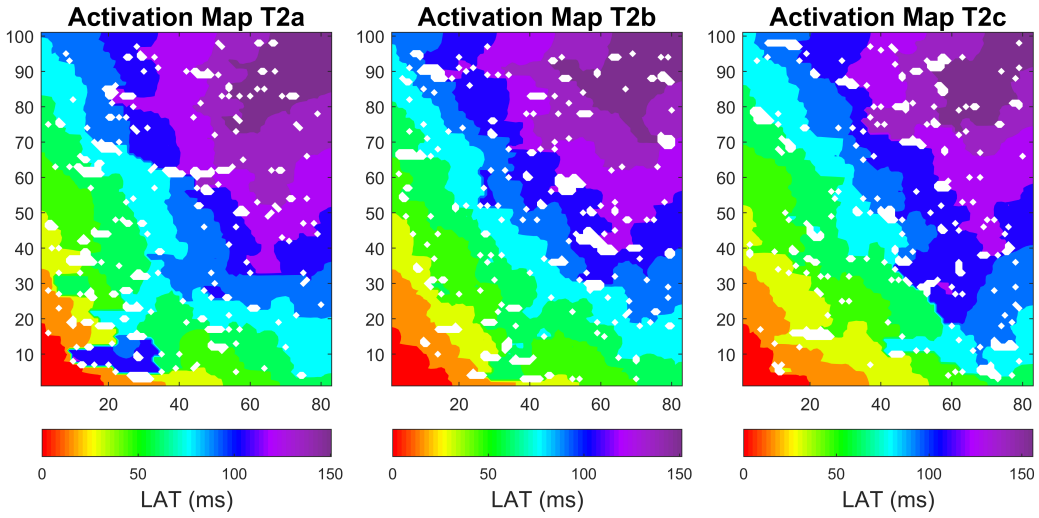

(a) (b) (c)

Figure 5.4: Single stimulation point simulated activation maps of (a) the first variation of tissue type T2, (b) the second variation of tissue type T2, and (c) the third variation of tissue type T2. The white spots represent cells that did not activate.

clinical data [50].

The transmembrane currents are estimated from EGMs using three distinct methods in this work. The first method involves using the deconvolution algorithm as described in [12], the second method involves using OLS, and the third method uses RLS. Furthermore, the method for estimating the LATs using SD on the EGMs is titled SD_{ϕ}. The EGMs are smoothed using a moving average Loess window of size 15 prior to LATs estimation. The LATs are computed using the SD method on both EGMs and estimated transmembrane

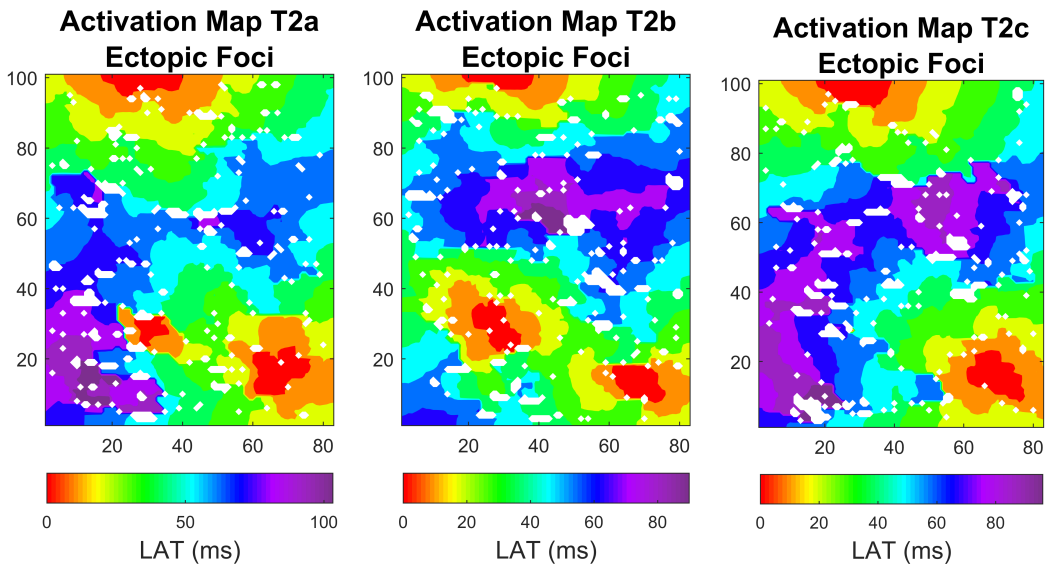

(a) (b) (c)

Figure 5.5: Ectopic foci simulated activation maps of (a) the first variation of tissue type T2, (b) the second variation of tissue type T2, and (c) the third variation of tissue type T2. The white spots represent cells that did not activate.

currents. The LATs estimated from the computed transmembrane currents are derived using $SD-Decon_I$, $SD-OLS_I$, and $SD-RLS_I$, for the deconvolution, OLS, and RLS transmembrane current estimation models, respectively. The deconvolution algorithm uses smoothed EGMs to estimate the transmembrane currents, while for the OLS and RLS algorithms, this proved to have negative effects, as certain components of the EGMs that were important for the estimation were lost after smoothing. However, the currents estimated using RLS and OLS are filtered using the PCMRA and SWT methods before LAT estimation.

While only a single conductivity map is used for tissue type T1 since it corresponds to healthy tissue and no other variations exist, for tissue type T2 three randomly generated variations are used to test how the algorithms perform in different scenarios. Furthermore, for each transmembrane current and LAT estimation experiment involving the OLS and RLS methods, wavelets with different supports (number of vanishing moments) are tested in order to observe how this influences the estimated transmembrane current filtering and consequently the LATs estimation. The number of vanishing moments (NoVM) used for PCMRA and SWT is the same for each iteration, as using different NoVM for filtering with PCMRA and then SWT did not yield relevant results, but rather most often increased the estimation errors. This might happen since by changing the support of the wavelet between PCMRA and SWT, the signal features are separated differently during the expansion and thus filtered differently, yielding an inaccurate signal. However, this is still subject to future testing.

The performance of transmembrane current estimation is evaluated using dynamic time warping (DTW). This is an efficient method for measuring the similarity between two temporal signals that are different in time or speed. DTW accomplishes this feat by matching every point from the first time series to one or more from the second time

series and the other way around, the first points from each of the two series have to be matched, but not necessarily to only themselves, same goes with the ending points of the two time series, and finally the mapping between the two series has to be monotonically increasing (no cross-matching between points from the two signals). In summary, the two time series are stretched across a common time frame such that their points are matched by minimizing the Euclidean distance between them. The result of DTW is the minimum distance between the two signals. This metric is great for evaluating the symmetry between the ground truth currents and the estimated currents, since their sampling rates differ because the EGMs are downsampled to match a 1kHz frequency and are thus shorter in length. The currents estimated using deconvolution are left out of this part since the main focus of this method is to only single out the main slope of the transmembrane current which corresponds to the cell depolarization and inherently the LAT, thus the estimated currents are far from resembling the shape of the initial simulated transmembrane currents [12]. These will only be compared in terms of LATs estimation. Furthermore, to evaluate the LATs estimation performance, the mean RMSE is used between the estimated LATs and the ground truth LATs.

5.2 Single Depolarization Wavefront

The first configuration used to simulate EGMs, and estimate LATs and transmembrane currents consists of stimulating the tissue from a single point, as depicted in Figures 5.1 and 5.2 by the purple hexagram. The estimation performance for transmembrane currents and LATs is evaluated for both tissue types. First, the transmembrane current estimation is evaluated using DTW between the estimated values and the ground truth, along with signal examples at certain points on the tissue grid. For OLS and RLS estimation, the DTW is computed per each NoVM used for the wavelet decompositions in PCMRA and then SWT. This is then followed by evaluating the LATs estimation performance for each of the SD_{ϕ}, $SD - Decon_I$, $SD - OLS_I$, and $SD - RLS_I$ estimation methods. Moreover, for OLS and RLS, the LATs estimations are evaluated at each NoVM.

5.2.1 Tissue type T1

The first analyzed tissue type is T1, where no conduction blocks are present, also known as fully healthy tissue. First, the transmembrane current estimation performance is analyzed with the help of the DTW, as explained in the previous paragraph.

The first method used to estimate transmembrane currents for tissue type T1 is OLS. The mean DTW value between the ground truth currents and the raw estimated currents based on the simulated EGMs is 3.805. The second method used to estimate transmembrane currents for tissue type T1 is RLS, which yields an average DTW of 3.484 for the raw initial estimations. The mean DTW value between the ground truth currents and the EGMs is 7.563. Furthermore, the DTW values evaluated after each filtering phase per NoVM can be observed in Figure 5.6a for the OLS method and in Figure 5.6b for the RLS method. Finally, a summary containing the mean DTW values based on the raw estimations, and the best mean DTW values after each filtering phase per each estimation method can be observed in Table 5.1. The best mean DTW values after each filtering phase are accompanied by the corresponding NoVM at which they were evaluated.

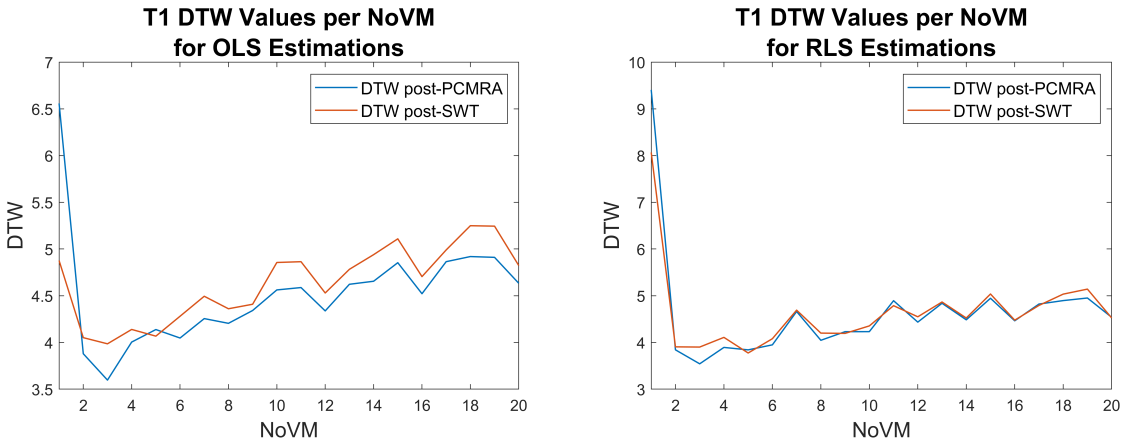

(a) (b)

Figure 5.6: DTW between ground truth transmembrane currents and estimated transmembrane currents of tissue type T1 after filtering by PCMRA and then SWT for (a) OLS estimations and (b) RLS estimations.

Table 5.1: Mean DTW values for tissue type T1 between the ground truth simulated transmembrane currents and the transmembrane current estimations using OLS and RLS (initial estimations, after PCMRA, and after both PCMRA and SWT filtering). The DTW values for the filtered estimations are the lowest computed over the 20 iterations of the NoVM. The amount of vanishing moments for which the best DTW value was obtained is displayed in brackets after the DTW values in the Table.

Step \ Method	OLS	RLS
Initial Estimation	3.805	3.484
Post-PCMRA(NoVM)	3.597(3)	3.542(3)
Post-SWT(NoVM)	3.985(3)	3.774(5)

Although the mean DTW values do not differ too much from one another, the RLS initial estimation is the most accurate. With T1 tissue resembling ideal conditions, the initial estimations are already satisfactory, however, the constrained version of least squares performs better in this case, while the OLS estimations still need to be filtered by PCMRA to yield a better DTW value. This happens due to the fact that OLS estimations could contain more artifacts than RLS, since the OLS optimization problem is underdetermined and no regularization is applied. Since certain signal components are left out for the fully filtered versions (PCMRA and SWT) when reconstructing the signal from the wavelet decomposition, their DTW values are the lowest. Moreover, the main trend shows that as the wavelet support increases, the MSE increases. Tissue type T1 resembles fully healthy and conductive tissue, with all cells being activated by the depolarization wave, meaning all electrodes record only the contributions of the cell(s) underneath them and the current estimations are already accurate enough. When performing PCMRA and SWT filtering, high-frequency information is removed, more specifically the first two finest decomposition levels are trimmed. As the wavelet support increases, the decomposition may gradually include more details connected with the main activation complex in the first two finest levels. Hence, the filtered estimations mainly resemble less the shape of the initially simulated currents. The irregularly high values at the beginning of the plots in Figure 5.6

Table 5.2: Mean DTW values for tissue type T1 between the ground truth simulated transmembrane currents and the transmembrane current estimations using OLS and RLS, for the signals filtered by removing only the finest decomposition level.

Step \ Method	OLS	RLS
Post-PCMRA(NoVM)	3.597(3)	3.172(3)
Post-SWT(NoVM)	3.985(3)	2.995(5)

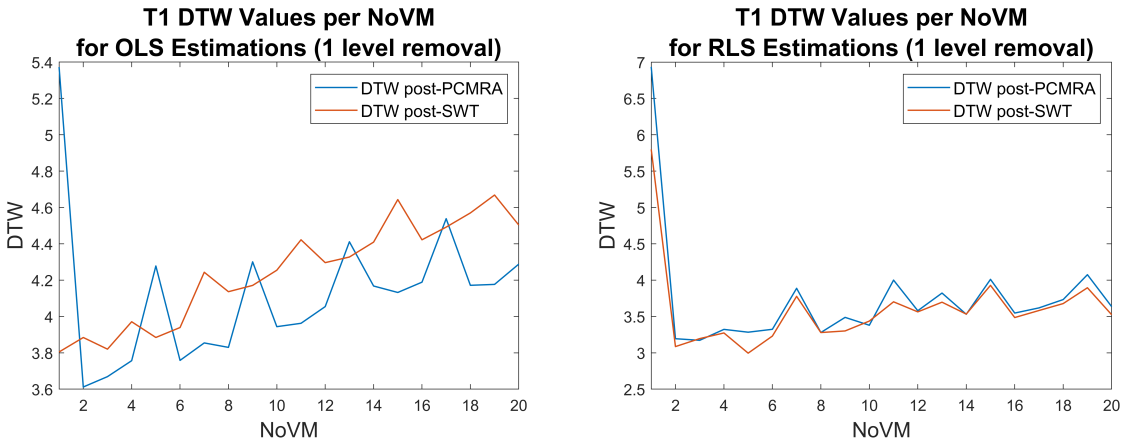

(a) (b)

Figure 5.7: DTW between ground truth transmembrane currents and estimated transmembrane currents of tissue type T1 after filtering by PCMRA and then SWT, by removing only the first finest level of the decomposition, for (a) OLS estimations and (b) RLS estimations.

are caused by the fact that the *sym*1 wavelet resembles the shape of a rectangular pulse, hence, the reconstructed signals have sharper, more rectangular shapes.

If removing the contributions of the first two finest decomposition levels causes the reconstructed signals to be less similar to the ground truth currents, removing only the first finest level of the decomposition can improve the similarity between signals. This happens as more information related to the main activation complex is included in the reconstruction and contrary to not removing any levels of the decomposition at all, removes any artifacts that might result from the current estimation process. The improved DTW values for the estimated signals filtered by only removing one level of the decomposition can be observed in Table 5.2. In addition, the DTW values evaluated after each filtering phase per NoVM can be observed in Figure 5.7a for the OLS method and in Figure 5.7b for the RLS method.

Although the same ascending trend that is displayed in the plots of Figure 5.6 can be observed in the plots of Figure 5.7, the DTW values are lower this time, since more high-frequency information is used for the signal reconstruction. It can also be seen that RLS-related estimations are more similar to the ground truth than OLS-related estimations. Following these results, for the LATs estimation step, only the first finest level of the decomposition is removed while filtering the estimated transmembrane currents.

The next step in the algorithm is LATs estimation using SD. A summary containing the best LATs estimation performance for the wavelet-filtered estimated currents using OLS and RLS, and the LATs estimated directly on the smoothed EGMs and the transmem-

Table 5.3: RMSE values for tissue type T1 between the ground truth simulated LATs and the estimated LATs based on the EGMs and transmembrane current estimations using deconvolution, OLS and RLS (initial estimations, after PCMRA, and after both PCMRA and SWT filtering). The RMSEs for the LATs obtained from the filtered estimated currents are the lowest values computed over the 20 iterations of the NoVM. The amount of vanishing moments for which the best RMSE was obtained is displayed in brackets after the RMSEs in the Table.

Method / Step	SD_ϕ	$SD - Decon_I$	$SD - OLS_I$	$SD - RLS_I$
Initial Estimation	0.385	0.422	0.655	0.882
Post-PCMRA(NoVM)	-	-	0.558(20)	0.584(16)
Post-SWT(NoVM)	-	-	0.571(5)	0.551(12)

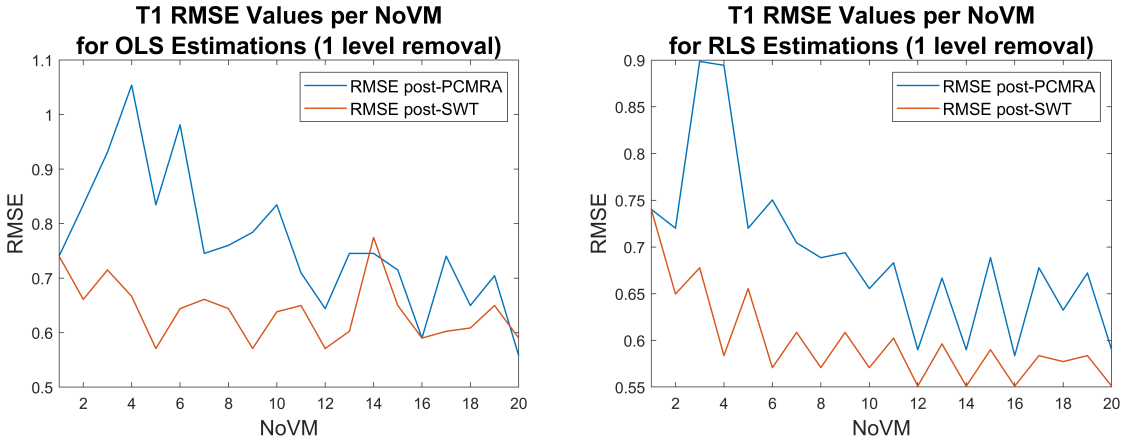

(a) (b)

Figure 5.8: RMSE between ground truth LATs and estimated LATs of tissue type T1 after filtering the estimated currents by PCMRA and then SWT for (a) OLS estimations and (b) RLS estimations.

brane currents estimated using deconvolution can be observed in Table 5.3. Moreover, for the LATs estimated on the filtered transmembrane currents, the corresponding NoVM for which the best performance was attained is displayed after the RMSE value in brackets. A full representation of how the LATs estimations RMSEs look per each NoVM iteration can be observed in Figure 5.8a and Figure 5.8b for the OLS and RLS estimated currents, respectively.

Based on the results presented in Table 5.3 it can be concluded that using the SD_ϕ LATs estimation produces the best outcome. Since the tissue on which the transmembrane currents are simulated is ideal, the smoothed EGMs are already accurate enough to estimate the LATs, as no parasitic components are present. Therefore, this means that the stronger the cell activation AP signal is for the cells under the electrode, in this case because the tissue is healthy, the more accurate the EGM is, and hence the LATs estimation is better. All three other methods perform worse than SD_ϕ as certain temporal and signal morphology information is translated during the current estimation optimization problems. Furthermore, for both $SD-OLS_I$ and $SD-RLS_I$ the PCMRA filtering gradually improves the LATs estimation for wavelets with larger and larger support, which can be seen in Figure 5.8, as the single main activation complex is better separated from other signal components. Further filtering the estimated currents by SWT seems to improve the

$SD - RLS_I$ LATs estimation. Nonetheless, for $SD - OLS_I$ estimations, further removing high-frequency information by applying SWT as well after PCMRA proves to have a minimal effect, as the best LAT result seems to be slightly worse than the PCMRA-only filtered estimation result. As a concluding remark, all RMSEs in Table 5.3 are lower than 1, consequently to the fact that most LATs estimation errors that stem from the 135 estimated currents per each method revolve around 0ms and ±1ms, with only a minor amount of outliers of ±2ms.

5.2.2 Tissue type T2

The second tissue type to be analyzed is T2, where conduction blocks are present in the form of lines and dots, simulating diseased tissue. Hence, the EGMs generated in tissue T2 are fractionated as explained in Section 3.1.2 of Chapter 3. In order to study how the estimation algorithms perform on different set-ups, three random variations of tissue type T2 are used as detailed at the beginning of this chapter. The transmembrane current estimation performance is first analyzed for each variation, followed by studying the LATs estimation performance. Even though for tissue type T1 only the first finest level of the wavelet decomposition was removed during filtering, for tissue type T2 this does not suffice, as in the majority of the cases the EGMs are heavily fractionated and contain estimation artifacts. Therefore, when filtering estimated transmembrane currents generated based on tissue type T2, the first two finest levels of the wavelet decomposition are removed, as this proved to produce better results in terms of LATs estimation as well.

The results of the similarity analysis between the ground truth currents and the estimated currents for each of the three variations of tissue T2 can be seen in Table 5.4. In addition, the mean DTW values between the ground truth currents and the EGMs are 6.067, 7.062, and 6.058, for tissues T2a, T2b, and T2c, respectively. It can be observed that although in some cases PCMRA filtering improves the DTW values, especially for RLS estimations, on average wavelet filtering does not greatly help with improving the similarity between the ground truth currents and estimated currents for diseased tissues. Furthermore, Figure 5.9 displays how the mean DTW values vary for each NoVM that was tested for both the OLS and RLS estimated transmembrane currents filtering per each variation of tissue T2. A similar trend can be observed as was seen for the T1 tissue, however, in this case, the spikes and troughs of the plots are much more prominent. This shows how certain wavelet supports help in separating certain signal parameters better than others, which also depends on the complexity and definition of the decomposed signals.

The main LATs estimation results can be observed in Table 5.5 for each tissue variation, and each current estimation and filtering method. Generally, the unfiltered versions of OLS and RLS perform worse. However, RMSEs obtained from the LATs based on filtered estimations are better, with the exception of tissue T2b, where the deconvolution-based estimations yielded a better LATs RMSE. In the plots of Figure 5.10, it can be seen that there is not one best support size and that no actual trends can be derived. Certain wavelet support sizes manage to isolate more parasitic components better in the finest levels and separate the main activation complex of the signals in the remaining decomposition levels than others. A single wavelet cannot be the most optimal for all 135 signals that stem from the electrode matrix. Hence, in some cases, heavily fractionated EGMs might still yield outliers after the estimation and filtering of the transmembrane currents. In other

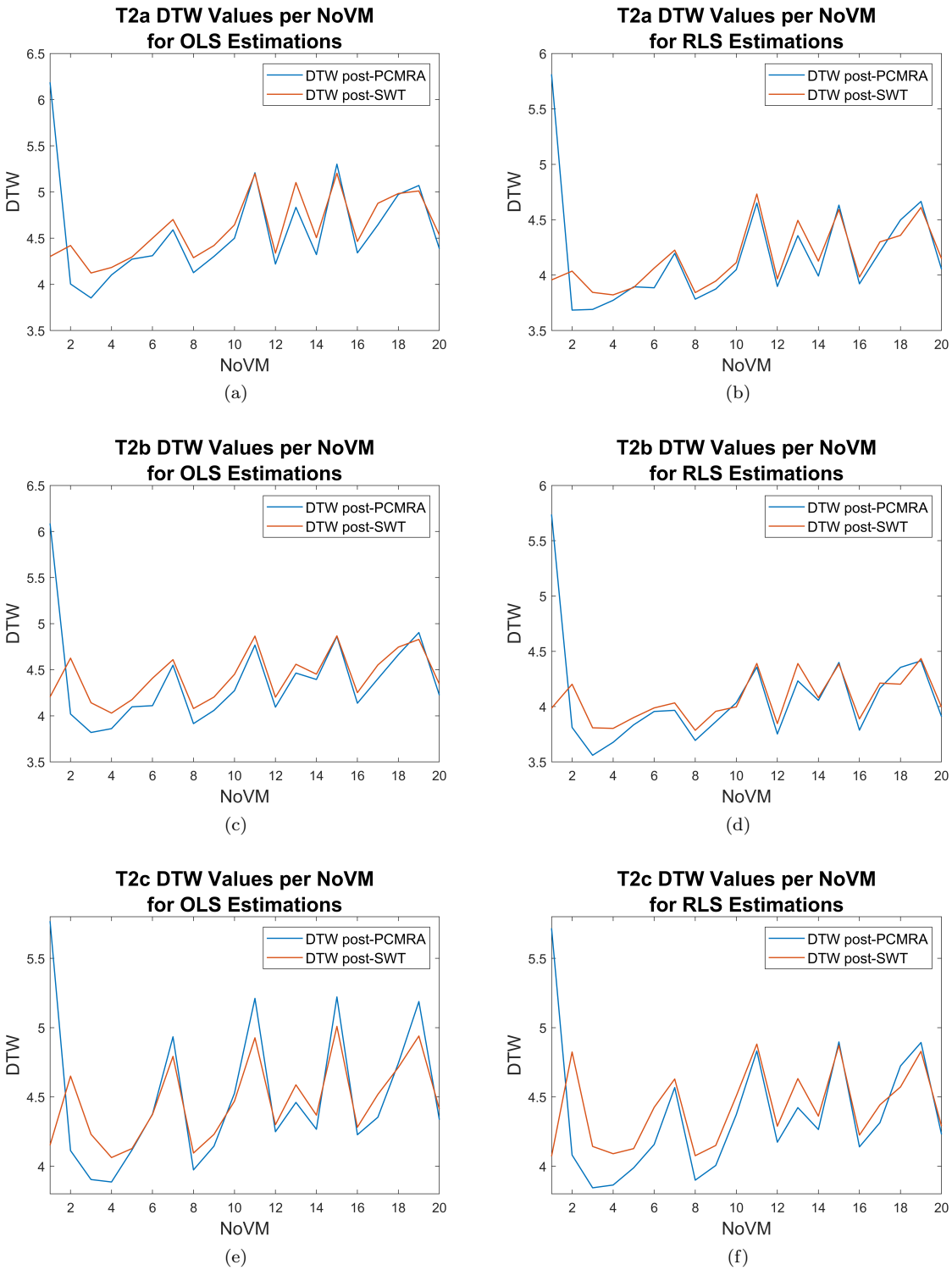

Figure 5.9: DTW between ground truth transmembrane currents and estimated transmembrane currents of tissue type T2 after filtering by PCMRA and then SWT for (a) OLS estimations of tissue T2a, (b) RLS estimations of tissue T2a, (c) OLS estimations of tissue T2b, (d) RLS estimations of tissue T2b, (e) OLS estimations of tissue T2c, and (f) RLS estimations of tissue T2c.

Table 5.4: Mean DTW values for the tissue type T2 variations between the ground truth simulated transmembrane currents and the transmembrane current estimations using OLS and RLS (initial estimations, after PCMRA, and after both PCMRA and SWT filtering). The DTW values for the filtered estimations are the lowest computed over the 20 iterations of the NoVM. The amount of vanishing moments for which the best DTW value was obtained is displayed in brackets after the DTW values in the Table.

Tissue →	T2a		T2b		T2c	
Method / Step	OLS	RLS	OLS	RLS	OLS	RLS
Initial Estimation	3.826	3.991	3.995	3.907	3.754	3.839
Post-PCMRA(NoVM)	3.853(3)	3.684(2)	3.819(3)	3.560(3)	3.886(4)	3.844(3)
Post-SWT(NoVM)	4.123(3)	3.823(4)	4.023(4)	3.786(8)	4.062(4)	4.072(1)

Table 5.5: RMSE values for the tissue type T2 variations between the ground truth simulated LATs and the estimated LATs based on the EGMs and transmembrane current estimations using deconvolution, OLS and RLS (initial estimations, after PCMRA, and after both PCMRA and SWT filtering). The RMSEs for the LATs obtained from the filtered estimated currents are the lowest values computed over the 20 iterations of the NoVM. The amount of vanishing moments for which the best RMSE was obtained is displayed in brackets after the RMSEs in the Table.

Tissue	Method / Step	SD_ϕ	$SD - Decon_I$	$SD - OLS_I$	$SD - RLS_I$
T2a	Initial Estimation	2.801	2.876	2.670	2.606
	Post-PCMRA(NoVM)	-	-	2.787(9)	1.701(20)
	Post-SWT(NoVM)	-	-	2.713(5)	1.481(12)
T2b	Initial Estimation	3.115	1.558	3.658	3.215
	Post-PCMRA(NoVM)	-	-	2.191(7)	1.775(8)
	Post-SWT(NoVM)	-	-	1.808(7)	1.613(6)
T2c	Initial Estimation	5.173	4.772	5.453	5.000
	Post-PCMRA(NoVM)	-	-	2.736(8)	2.080(8)
	Post-SWT(NoVM)	-	-	2.382(8)	1.927(8)

cases, although beneficial for most estimated transmembrane currents, the wavelet filtering might remove relevant signal components from other estimated currents, which can lead to bad LAT estimations and consequently a higher RMSE.

5.3 Triple Depolarization Wavefront

The second configuration used to simulate EGMs, and estimate LATs and transmembrane currents consists of stimulating the tissue from three different points, as depicted in Figures 5.1 and 5.2 by the orange hexagrams. The estimation performance for transmembrane currents and LATs is evaluated for both tissue types. First, the transmembrane current estimation is evaluated using DTW between the estimated values and the ground truth, along with signal examples at certain points on the tissue grid. For OLS and RLS estimation, the DTW is computed per each NoVM used for the wavelet decompositions in PCMRA and then SWT. This is then followed by evaluating the LATs estimation performance for each of the SD_ϕ, $SD - Decon_I$, $SD - OLS_I$, and $SD - RLS_I$ estimation methods. Moreover, for OLS and RLS, the LATs estimations are evaluated at each NoVM. For tissue type T1 only the first finest decomposition level is removed during wavelet filtering, while for the tissue type T2 variations the first two finest are removed, as explained in the previous section for the single depolarization wavefront configuration.

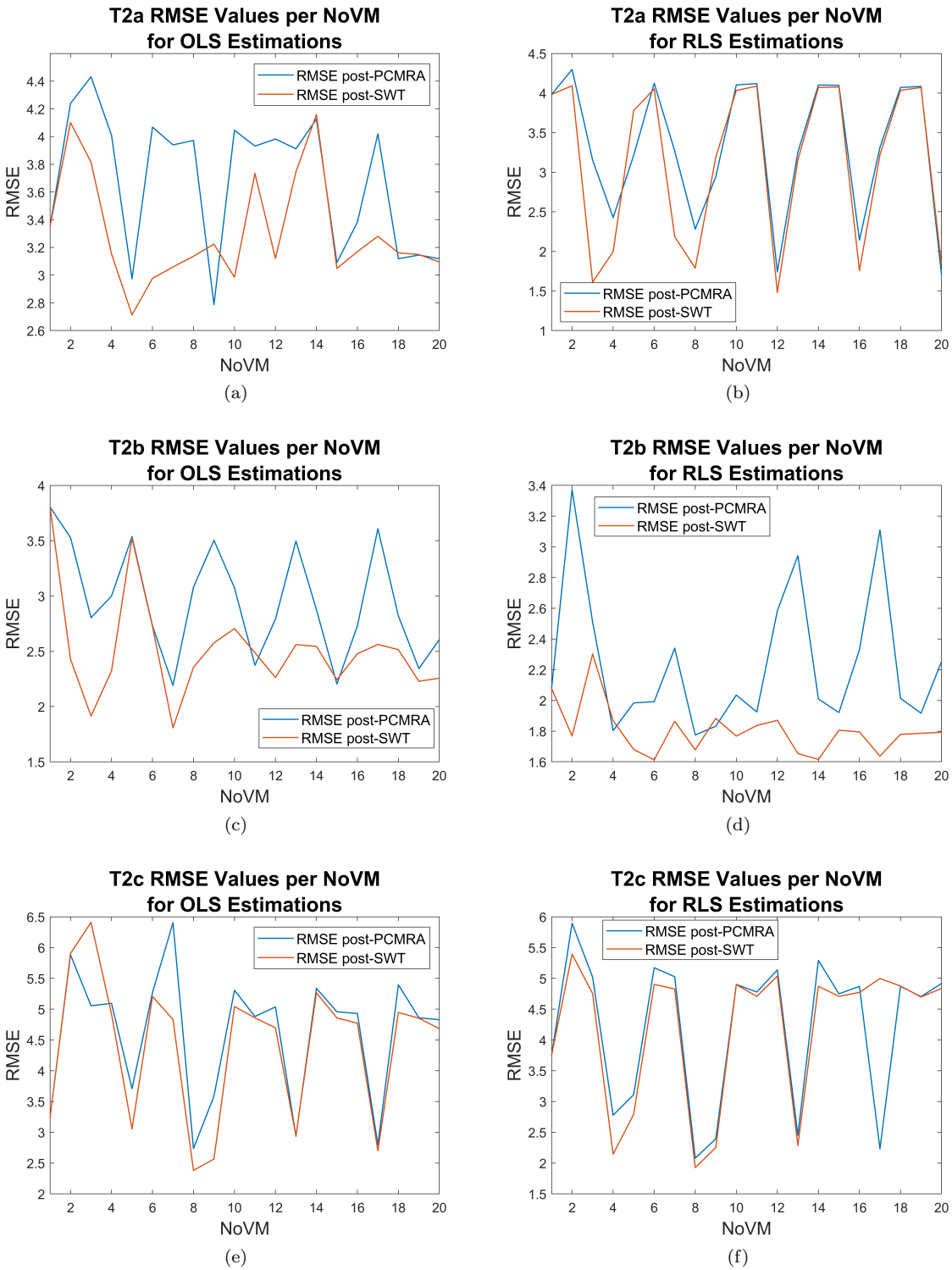

Figure 5.10: RMSE between ground truth LATs and estimated LATs of tissue type T2 after filtering the estimated currents by PCMRA and then SWT for (a) OLS estimations of tissue T2a, (b) RLS estimations of tissue T2a, (c) OLS estimations of tissue T2b, (d) RLS estimations of tissue T2b, (e) OLS estimations of tissue T2c, and (f) RLS estimations of tissue T2c.

Table 5.6: Mean DTW values for tissue type T1 (triple stimulation) between the ground truth simulated transmembrane currents and the transmembrane current estimations using OLS and RLS (initial estimations, after PCMRA, and after both PCMRA and SWT filtering). The DTW values for the filtered estimations are the lowest computed over the 20 iterations of the NoVM. The amount of vanishing moments for which the best DTW value was obtained is displayed in brackets after the DTW values in the Table.

Step \ Method	OLS	RLS
Initial Estimation	5.808	4.965
Post-PCMRA(NoVM)	5.708(3)	4.907(3)
Post-SWT(NoVM)	6.533(3)	5.008(9)

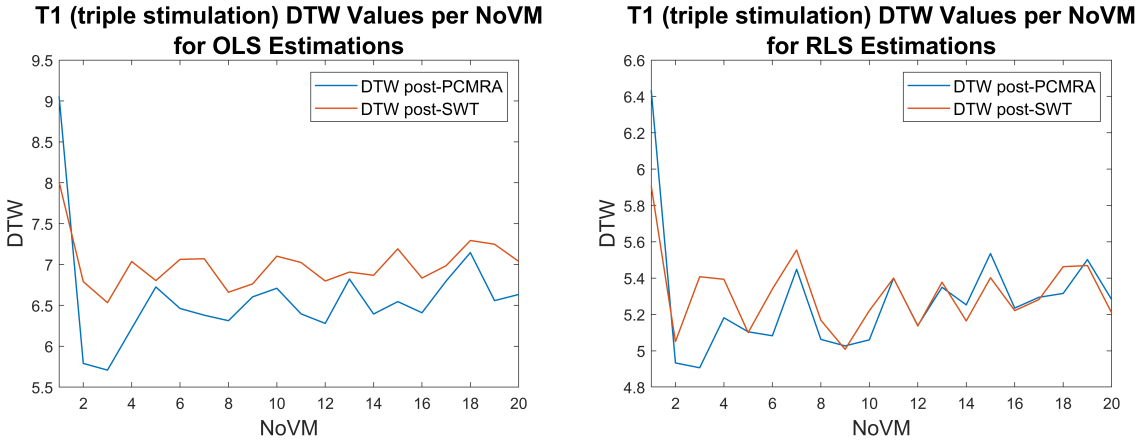

(a) (b)

Figure 5.11: DTW between ground truth transmembrane currents and estimated transmembrane currents of tissue type T1 (triple stimulation) after filtering by PCMRA and then SWT for (a) OLS estimations and (b) RLS estimations.

5.3.1 Tissue Type T1

The results of the similarity analysis between the ground truth currents and the estimated currents for tissue type T1 for the triple depolarization wavefront configuration can be seen in Table 5.6. In addition, the mean DTW value between the ground truth currents and the EGMs is 9.132. Furthermore, Figure 5.11 displays how the mean DTW values vary for each NoVM that was tested for both the OLS and RLS estimated transmembrane currents filtering for tissue type T1. The same principal observations can be made here as were done for the single depolarization wavefront case.

The main LATs estimation results can be observed in Table 5.7 for tissue type T1, per each current estimation and filtering method. Moreover, a full representation of how the LATs estimations RMSEs look per each NoVM iteration can be observed in Figure 5.12a and Figure 5.12b for the OLS and RLS estimated currents, respectively. Once again, the same observation can be made as the ones mentioned in the single depolarization wavefront case, although this time the RMSE values are mainly closer in range to one another, meaning the OLS and RLS perform better in this case.

Table 5.7: RMSE values for tissue type T1 (triple stimulation) between the ground truth simulated LATs and the estimated LATs based on the EGMs and transmembrane current estimations using deconvolution, OLS and RLS (initial estimations, after PCMRA, and after both PCMRA and SWT filtering). The RMSEs for the LATs obtained from the filtered estimated currents are the lowest values computed over the 20 iterations of the NoVM. The amount of vanishing moments for which the best RMSE was obtained is displayed in brackets after the RMSEs in the Table.

Method / Step	SD_{ϕ}	$SD - Decon_I$	$SD - OLS_I$	$SD - RLS_I$
Initial Estimation	0.404	0.494	0.577	0.899
Post-PCMRA(NoVM)	-	-	0.571(20)	0.584(20)
Post-SWT(NoVM)	-	-	0.531(12)	0.571(16)

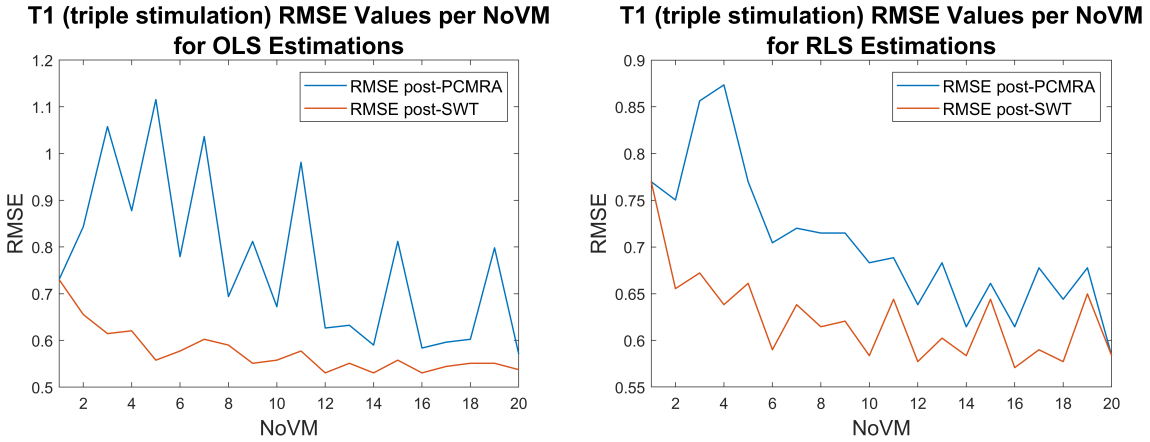

(a) (b)

Figure 5.12: RMSE between ground truth LATs and estimated LATs of tissue type T1 (triple stimulation) after filtering the estimated currents by PCMRA and then SWT for (a) OLS estimations and (b) RLS estimations.

5.3.2 Tissue Type T2

The results of the similarity analysis between the ground truth currents and the estimated currents for each of the three variations of tissue T2 for the triple depolarization wavefront configuration can be seen in Table 5.8. In addition, the mean DTW values between the ground truth currents and the EGMs are 6.498, 6.504, and 6.236, for tissues T2a, T2b, and T2c, respectively. Furthermore, Figure 5.13 displays how the mean DTW values vary for each NoVM that was tested for both the OLS and RLS estimated transmembrane currents filtering per each variation of tissue T2. The same principal observations can be made here as were done for the single depolarization wavefront case.

The main LATs estimation results can be observed in Table 5.9 for each of the three variations of tissue T2, per each current estimation and filtering method. In the plots of Figure 5.14, it can be seen once again that there is not one best support size and that no actual trends can be derived, as mentioned for the single depolarization wavefront configuration as well. Moreover, it can be seen in Figure 5.14a and Figure 5.14c that for a NoVM of 1, the RMSE values are abnormally high. This might be caused by the fact that since the wavelet support is too small, and electrodes record AP influences from three different stimulation points, the relevant features of the signal could be included

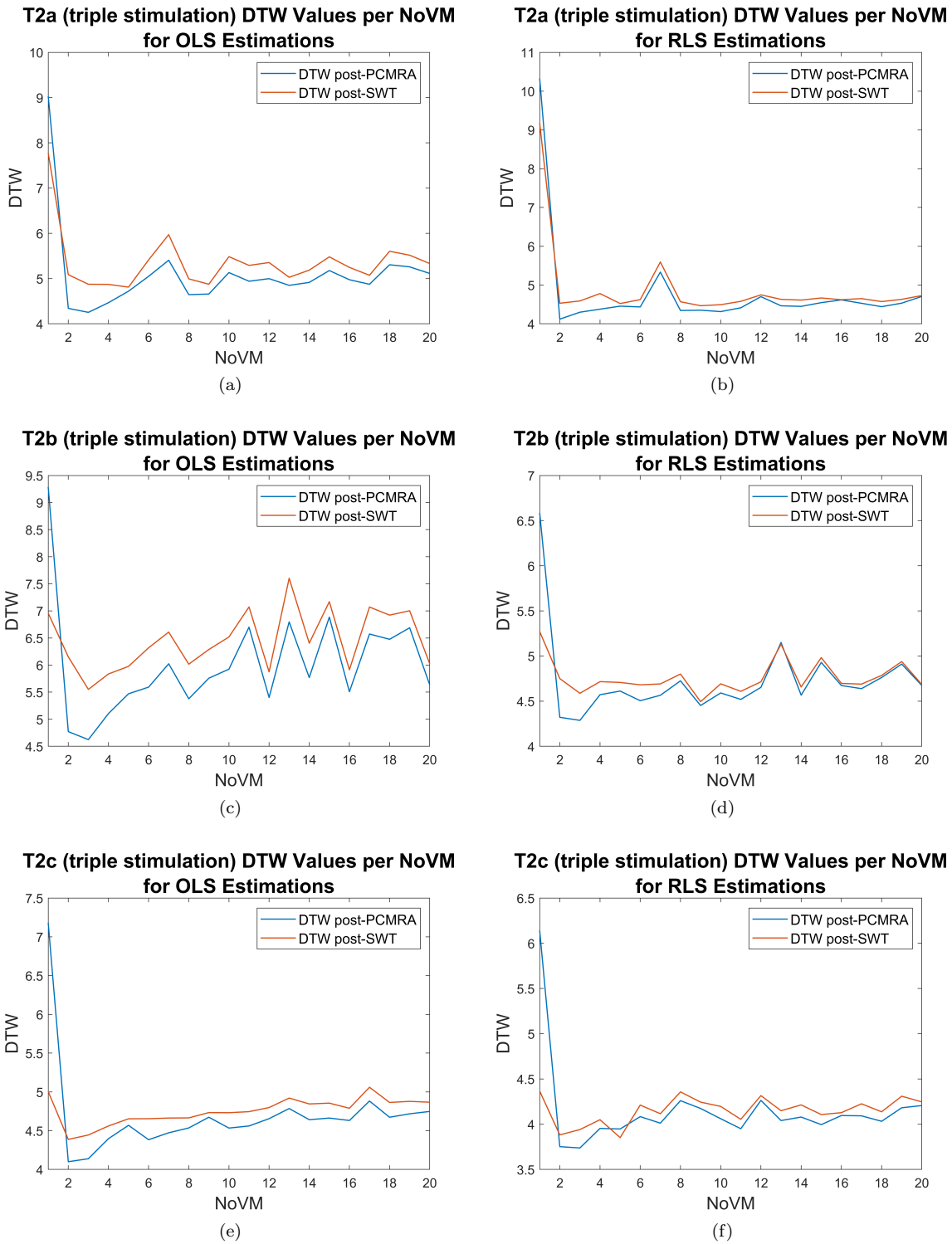

Figure 5.13: DTW between ground truth transmembrane currents and estimated transmembrane currents of tissue type T2 (triple stimulation) after filtering by PCMRA and then SWT for (a) OLS estimations of tissue T2a, (b) RLS estimations of tissue T2a, (c) OLS estimations of tissue T2b, (d) RLS estimations of tissue T2b, (e) OLS estimations of tissue T2c, and (f) RLS estimations of tissue T2c.

Table 5.8: Mean DTW values for the tissue type T2 (triple stimulation) variations between the ground truth simulated transmembrane currents and the transmembrane current estimations using OLS and RLS (initial estimations, after PCMRA, and after both PCMRA and SWT filtering). The DTW values for the filtered estimations are the lowest computed over the 20 iterations of the NoVM. The amount of vanishing moments for which the best DTW value was obtained is displayed in brackets after the DTW values in the Table.

Tissue →	T2a		T2b		T2c	
Method / Step	OLS	RLS	OLS	RLS	OLS	RLS
Initial Estimation	4.330	4.401	5.108	4.450	4.053	4.028
Post-PCMRA(NoVM)	4.253(3)	4.120(2)	4.623(3)	4.287(3)	4.100(2)	3.737(3)
Post-SWT(NoVM)	4.810(5)	4.466(9)	5.550(3)	4.495(9)	4.387(2)	3.852(5)

Table 5.9: RMSE values for the tissue type T2 (triple stimulation) variations between the ground truth simulated LATs and the estimated LATs based on the EGMs and transmembrane current estimations using deconvolution, OLS and RLS (initial estimations, after PCMRA, and after both PCMRA and SWT filtering). The RMSEs for the LATs obtained from the filtered estimated currents are the lowest values computed over the 20 iterations of the NoVM. The amount of vanishing moments for which the best RMSE was obtained is displayed in brackets after the RMSEs in the Table.

Tissue	Method / Step	SD_ϕ	$SD - Decon_I$	$SD - OLS_I$	$SD - RLS_I$
T2a	Initial Estimation	3.057	2.505	2.552	5.421
	Post-PCMRA(NoVM)	-	-	1.789(17)	1.529(7)
	Post-SWT(NoVM)	-	-	1.215(17)	1.321(16)
T2b	Initial Estimation	5.597	2.833	5.826	5.787
	Post-PCMRA(NoVM)	-	-	3.123(14)	3.084(6)
	Post-SWT(NoVM)	-	-	3.026(8)	2.992(6)
T2c	Initial Estimation	5.350	3.427	4.363	4.608
	Post-PCMRA(NoVM)	-	-	3.676(19)	2.539(15)
	Post-SWT(NoVM)	-	-	2.935(9)	2.508(20)

with parasitic components in the first two decomposition levels and thus are removed. Otherwise, it can be observed for this configuration as well that a higher NoVM leads to better results.

The LATs estimation performance is more diverse here, as in each case a different method performs better. However, whereas the RLS-based results are the best for only tissue T2c, they are really close in range to the best RMSE values computed for the other two tissues. This shows that once again on average the RLS-based estimations display a better performance, similar to the single depolarization wavefront configuration.

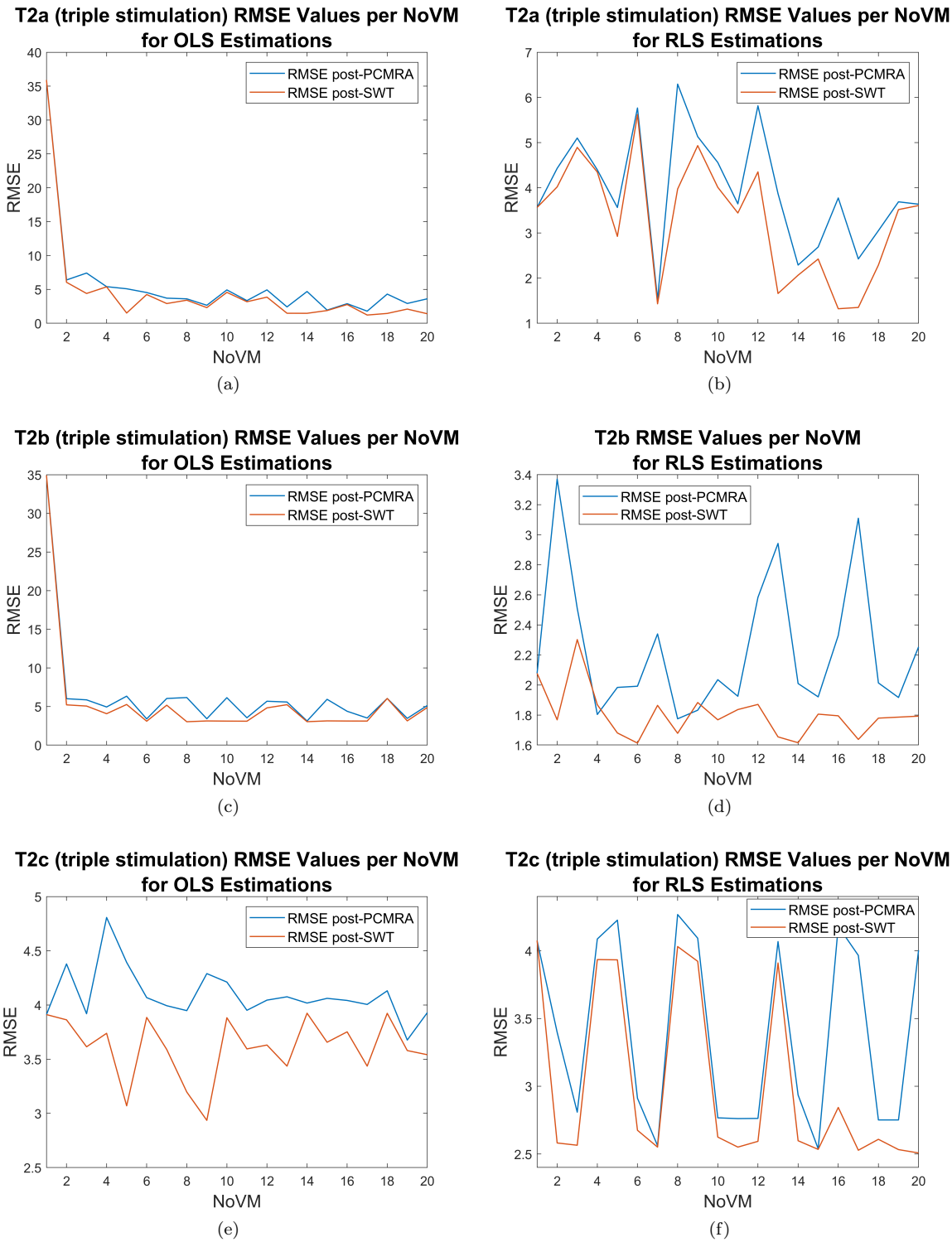

Figure 5.14: RMSE between ground truth LATs and estimated LATs of tissue type T2 (triple stimulation) after filtering the estimated currents by PCMRA and then SWT for (a) OLS estimations of tissue T2a, (b) RLS estimations of tissue T2a, (c) OLS estimations of tissue T2b, (d) RLS estimations of tissue T2b, (e) OLS estimations of tissue T2c, and (f) RLS estimations of tissue T2c.

6 Conclusion

The aim of this thesis was to analyze how accurate estimates of transmembrane currents could be computed using regression in the form of least squares. Furthermore, LATs estimation was looked into by computing the SD on the estimated transmembrane currents before and after applying certain filters in the form of wavelet decompositions and PCA.

This being said, two transmembrane current estimation methods have been introduced, OLS, which represents the standard version of least squares, and RLS, which represents a regularized version of least squares, by using a combination of lasso and ridge regressions in the penalty term. The reason behind is to promote signal sparsity, while also dealing with multicollinearity.

In order to improve transmembrane current estimations and inherently LATs estimation, wavelet decompositions and PCA methods were introduced to show parasitic components can be separated from the main activation complex by performing a multiresolution analysis. Furthermore, it was shown how this process works and how it deals with a noisy estimation based on a noisy EGM as well.

Finally, these algorithms were tested for several simulation set-ups, namely for healthy tissue and disease tissue. In addition, for each tissue type, two stimulation configurations were used. One where only one stimulation point was used, at the bottom left of the cell grid, and a second one where three stimulation points were used along the cell grid. By testing on these set-ups, the performance of the detailed algorithms was analyzed and the effect of fractionated EGMs on all estimations was discussed.

The main ideas extracted from the simulation results are as follows. The OLS and RLS-based transmembrane current estimations are significantly more similar to the ground truth transmembrane currents than the EGMs are. On average, wavelet-filtered RLS-based estimations have slightly better performance, especially for LATs estimation. Nonetheless, in certain cases, wavelet-filtering still cannot improve the estimations, as the EGMs are heavily fractionated and outliers still persist in the signals. This causes the results to be higher than desired. It was also observed that in certain select tissue configurations, the OLS and RLS-based estimations were close in range to the deconvolution-based ones. Moreover, for healthy tissue, or generally tissue where the cells activation is powerful enough, *i.e.* the stimulation point is under the electrode matrix, and the recorded EGMs are thus already accurate, EGM denoising is merely sufficient before estimating the LATs directly on the EGMs. All in all, the size of the wavelet support is seen to matter in both transmembrane current estimations and LAT estimations. No one good universal support size could be found. This happens as signals have different morphologies and complexities, depending on the type of tissue and how obstructed the electric pathways are in the tissue. Even so, it can be seen that smaller support sizes help transmembrane current estimations be more similar to the ground truth transmembrane currents, since these separate closely-spaced parasitic contributions and artifacts better from the main activation complex details. In addition, bigger support sizes improve LAT estimations. Although they are more aggressive and eliminate more details from the currents that can

be found in the finest levels, since on average they make current estimations less similar to the ground truth, they are mainly better at isolating the maximum negative slope.

Having said this, some recommendations for future work can be made. A first line of future research would focus on the optimization of the α parameter in the RLS regression problem, by experimenting and systematically determining better values. Second, tests could be made on EGMs with biologically accurate added noise and equipment-specific added noise, to resemble real conditions better. Different anisotropy ratios could be used as well, since in real-life conditions, the depolarization wavefront might travel at different speeds on different axes. Regarding the wavelet decomposition, it was observed that removing higher frequency subspaces improves certain estimations, nonetheless, instead of completely removing those subspaces, thresholding methods could be used on all subspaces, in order to not lose relevant signal information. It was shown that if in certain cases less high-frequency information was removed, the estimations were better. Moreover, results showed different wavelet support sizes yield better results, thus, adaptive wavelets could be used to better fit the morphology of the decomposed signals. Finally, these algorithms should be tested on clinical data to test their performance in real-life conditions.

Bibliography

[1] OLI - Drawing Heart and great vessels from anterior - English labels" at AnatomyTOOL.org by Open Learning Initiative, license: Creative Commons Attribution-NonCommercial-ShareAlike.

[2] Diberri, Pacemaker cell action potential diagram, Online, license: Attribution-ShareAlike 3.0 Unported (CC BY-SA 3.0), `https://commons.wikimedia.org/wiki/File:Pacemaker_potential.svg`.

[3] A. Sved, Cardiac ventricular myocyte action potential, Online, license: Creative Commons Attribution-Share Alike 4.0 International, `https://commons.wikimedia.org/wiki/File:Cardiac_ventricular_myocyte_action_potential.png`.

[4] OLI - Drawing Cardiac conduction system and action potentials - English labels" at AnatomyTOOL.org by Open Learning Initiative, license: Creative Commons Attribution-NonCommercial-ShareAlike.

[5] A. Atkielski, Schematic diagram of normal sinus rhythm for a human heart as seen on ECG, Online, Public Domain, `https://commons.wikimedia.org/wiki/File:SinusRhythmLabels.svg`.

[6] B. Abdi, *Atrial fibrillation fingerprinting*. PhD thesis, Delft University of Technology, 2021.

[7] R. Starreveld-Brand, "Uncovering atrial fibrillation complexity: From signals to (bio) markers," 2021.

[8] Nrets, Circuit diagram of neuronal membrane based on Hodgkin and Huxley model, Online, license: Attribution-ShareAlike 3.0 Unported (CC BY-SA 3.0), `https://commons.wikimedia.org/wiki/File:MembraneCircuit.svg`.

[9] J. M. De Bakker and F. H. Wittkampf, "The pathophysiologic basis of fractionated and complex electrograms and the impact of recording techniques on their detection and interpretation," *Circulation: Arrhythmia and Electrophysiology*, vol. 3, no. 2, pp. 204–213, 2010.

[10] T. M. Munger, L. Q. Wu, and W. K. Shen, "Atrial fibrillation," *Journal of Biomedical Research*, vol. 28, no. 1, pp. 1–17, 2014.

[11] E. N. Prystowsky, B. J. Padanilam, and R. I. Fogel, "Treatment of atrial fibrillation," *Jama*, vol. 314, no. 3, pp. 278–288, 2015.

[12] B. Abdi, R. C. Hendriks, A. J. van der Veen, and N. M. de Groot, "Improved local activation time annotation of fractionated atrial electrograms for atrial mapping," *Computers in Biology and Medicine*, vol. 117, p. 103590, 2020.

[13] Elaine N. Marieb and Katja Hoehn, *Human Anatomy and Physiology, 11th Global Edition*. Harlow, United Kingdom: Pearson Education, Limited, 11th ed., 2019.

[14] I. D. Kotadia, J. Whitaker, C. H. Roney, S. Niederer, M. O'Neill, and M. Bishop, "Anisotropic Cardiac Conduction," *Arrhythmia & Electrophysiology Review 2020;9(4):202–10.*, 2020.

[15] A. L. . Goldberger, Z. D. Goldberger, and A. T. A. T. T. Shvilkin, *Goldberger's clinical electrocardiography : a simplified approach LK - https://tudelft.on.worldcat.org/oclc/986242877*. Philadelphia, PA: Elsevier, ninth edition. nv - 1 online resource (ix, 260, e98 pages) : illustrations (some color) ed., 2018.

[16] U. B. Tedrow and W. G. Stevenson, "Recording and interpreting unipolar electrograms to guide catheter ablation," *Heart Rhythm*, vol. 8, no. 5, pp. 791–796, 2011.

[17] M. Shenasa, G. Hindricks, D. J. Callans, J. M. Miller, and M. E. Josephson, "Cardiac Mapping, Fifth Edition," pp. 70–83, 2019.

[18] N. M. de Groot, M. A. Allessie, L. J. van der Does, and A. J. Bogers, "Atrial fibrillation from a unipolar, high-resolution perspective," *Cardiac Mapping*, pp. 343–350, 2019.

[19] C. D. Cantwell, C. H. Roney, F. S. Ng, J. H. Siggers, S. J. Sherwin, and N. S. Peters, "Techniques for automated local activation time annotation and conduction velocity estimation in cardiac mapping," *Computers in biology and medicine*, vol. 65, pp. 229–242, 2015.

[20] L. J. van der Does and N. M. de Groot, "Inhomogeneity and complexity in defining fractionated electrograms," *Heart rhythm*, vol. 14, no. 4, pp. 616–624, 2017.

[21] A. D. Ceornodolea, R. Bal, and J. L. Severens, "Epidemiology and Management of Atrial Fibrillation and Stroke: Review of Data from Four European Countries," *Stroke Research and Treatment*, vol. 2017, p. 8593207, 2017.

[22] M. K. Chung, L. L. Eckhardt, L. Y. Chen, H. M. Ahmed, R. Gopinathannair, J. A. Joglar, P. A. Noseworthy, Q. R. Pack, P. Sanders, K. M. Trulock, and null Null, "Lifestyle and Risk Factor Modification for Reduction of Atrial Fibrillation: A Scientific Statement From the American Heart Association," *Circulation*, vol. 141, pp. e750–e772, apr 2020.

[23] S. L. Kopecky, B. J. Gersh, M. D. McGoon, J. P. Whisnant, D. R. Holmes, D. M. Ilstrup, and R. L. Frye, "The Natural History of Lone Atrial Fibrillation," *New England Journal of Medicine*, vol. 317, pp. 669–674, sep 1987.

[24] M. M. Gallagher and A. J. Camm, "Classification of atrial fibrillation," 1997.

[25] T. Kato, T. Yamashita, K. Sagara, H. Iinuma, and L.-T. Fu, "Progressive nature of paroxysmal atrial fibrillation observations from a 14-year follow-up study," *Circulation Journal*, vol. 68, no. 6, pp. 568–572, 2004.

[26] S. Petrutiu, J. Ng, G. M. Nijm, H. Al-Angari, S. Swiryn, and A. V. Sahakian, "Atrial fibrillation and waveform characterization," *IEEE engineering in medicine and biology magazine*, vol. 25, no. 6, pp. 24–30, 2006.

[27] M. S. Guillem, A. M. Climent, M. Rodrigo, F. Fernández-Avilés, F. Atienza, and O. Berenfeld, "Presence and stability of rotors in atrial fibrillation: evidence and therapeutic implications," *Cardiovascular Research*, vol. 109, pp. 480–492, apr 2016.

[28] J. W. Waks and M. E. Josephson, "Mechanisms of Atrial Fibrillation - Reentry, Rotors and Reality.," *Arrhythmia & electrophysiology review*, vol. 3, pp. 90–100, aug 2014.

[29] N. de Groot, L. Van Der Does, A. Yaksh, E. Lanters, C. Teuwen, P. Knops, P. van de Woestijne, J. Bekkers, C. Kik, A. Bogers, *et al.*, "Direct proof of endo-epicardial asynchrony of the atrial wall during atrial fibrillation in humans," *Circulation: Arrhythmia and Electrophysiology*, vol. 9, no. 5, p. e003648, 2016.

[30] J. Jalife, O. Berenfeld, A. Skanes, and R. Mandapati, "Mechanisms of atrial fibrillation: mother rotors or multiple daughter wavelets, or both?," *Journal of cardiovascular electrophysiology*, vol. 9, no. 8 Suppl, pp. S2–12, 1998.

[31] H. Calkins, K. H. Kuck, R. Cappato, J. Brugada, A. J. Camm, S.-A. Chen, H. J. Crijns, R. J. Damiano Jr, D. W. Davies, J. DiMarco, *et al.*, "Expert consensus statement on catheter and surgical ablation of atrial fibrillation: recommendations for patient selection, procedural techniques, patient management, and follow-up," *Europace*, vol. 14, no. 4, pp. 528–606, 2012.

[32] L. F. Tops, M. J. Schalij, E. R. Holman, L. van Erven, E. E. van der Wall, and J. J. Bax, "Right ventricular pacing can induce ventricular dyssynchrony in patients with atrial fibrillation after atrioventricular node ablation," *Journal of the American College of Cardiology*, vol. 48, no. 8, pp. 1642–1648, 2006.

[33] H. Kottkamp, G. Hindricks, R. ü. Autschbach, B. Krauss, B. Strasser, P. Schirdewahn, A. Fabricius, G. Schuler, and F.-W. Mohr, "Specific linear left atrial lesions in atrial fibrillation: intraoperative radiofrequency ablation using minimally invasive surgical techniques," *Journal of the American College of Cardiology*, vol. 40, no. 3, pp. 475–480, 2002.

[34] T. Ashihara, R. Haraguchi, K. Nakazawa, T. Namba, T. Ikeda, Y. Nakazawa, T. Ozawa, M. Ito, M. Horie, and N. A. Trayanova, "The role of fibroblasts in complex fractionated electrograms during persistent/permanent atrial fibrillation: implications for electrogram-based catheter ablation," *Circulation research*, vol. 110, no. 2, pp. 275–284, 2012.

[35] I. Nault, S. Miyazaki, A. Forclaz, M. Wright, A. Jadidi, P. Jaïs, M. Hocini, and M. Haïssaguerre, "Drugs vs. ablation for the treatment of atrial fibrillation: the evidence supporting catheter ablation," *European heart journal*, vol. 31, no. 9, pp. 1046–1054, 2010.

[36] M. Courtemanche, R. J. Ramirez, and S. Nattel, "Ionic mechanisms underlying human atrial action potential properties: Insights from a mathematical model," *American Journal of Physiology - Heart and Circulatory Physiology*, vol. 275, no. 1 44-1, 1998.

[37] N. Virag, V. Jacquemet, C. S. Henriquez, S. Zozor, O. Blanc, J. M. Vesin, E. Pruvot, and L. Kappenberger, "Study of atrial arrhythmias in a computer model based on magnetic resonance images of human atria," *Chaos*, vol. 12, no. 3, pp. 754–763, 2002.

[38] R. Plonsey, R. C. Barr, and A. Bioelectricity, *Quantitative Approach*. Springer, 2007.

[39] M. S. Spach and P. C. Dolber, "Relating extracellular potentials and their derivatives to anisotropic propagation at a microscopic level in human cardiac muscle. evidence for electrical uncoupling of side-to-side fiber connections with increasing age.," *Circulation research*, vol. 58, no. 3, pp. 356–371, 1986.

[40] B. Abdi, R. C. Hendriks, A.-J. van der Veen, and N. M. de Groot, "A compact matrix model for atrial electrograms for tissue conductivity estimation," *Computers in biology and medicine*, vol. 107, pp. 284–291, 2019.

[41] E. J. Ciaccio, A. B. Biviano, W. Whang, A. Gambhir, and H. Garan, "Different characteristics of complex fractionated atrial electrograms in acute paroxysmal versus long-standing persistent atrial fibrillation," *Heart Rhythm*, vol. 7, no. 9, pp. 1207–1215, 2010.

[42] T. Goldstein and S. Osher, "The split bregman method for l1-regularized problems," *SIAM journal on imaging sciences*, vol. 2, no. 2, pp. 323–343, 2009.

[43] J. Friedman, T. Hastie, and R. Tibshirani, "Regularization paths for generalized linear models via coordinate descent," *Journal of statistical software*, vol. 33, no. 1, p. 1, 2010.

[44] C. S. Burrus, "Wavelets and wavelet transforms," *Rice University: https://hdl.handle.net/1911/112342*, 2015.

[45] B. R. Bakshi, "Multiscale pca with application to multivariate statistical process monitoring," *AIChE journal*, vol. 44, no. 7, pp. 1596–1610, 1998.

[46] R. R. Coifman and D. L. Donoho, *Translation-invariant de-noising*. Springer, 1995.

[47] J. E. Fowler, "The redundant discrete wavelet transform and additive noise," *IEEE Signal Processing Letters*, vol. 12, no. 9, pp. 629–632, 2005.

[48] V. Jacquemet and C. S. Henriquez, "Genesis of complex fractionated atrial electrograms in zones of slow conduction: a computer model of microfibrosis," *Heart rhythm*, vol. 6, no. 6, pp. 803–810, 2009.

[49] E. Vigmond, A. Pashaei, S. Amraoui, H. Cochet, and M. Hassaguerre, "Percolation as a mechanism to explain atrial fractionated electrograms and reentry in a fibrosis model based on imaging data," *Heart rhythm*, vol. 13, no. 7, pp. 1536–1543, 2016.

[50] A. Yaksh, L. J. van der Does, C. Kik, P. Knops, F. B. Oei, P. C. van de Woestijne, J. A. Bekkers, A. J. Bogers, M. A. Allessie, and N. M. de Groot, "A novel intra-operative, high-resolution atrial mapping approach," *Journal of Interventional Cardiac Electrophysiology*, vol. 44, pp. 221–225, 2015.